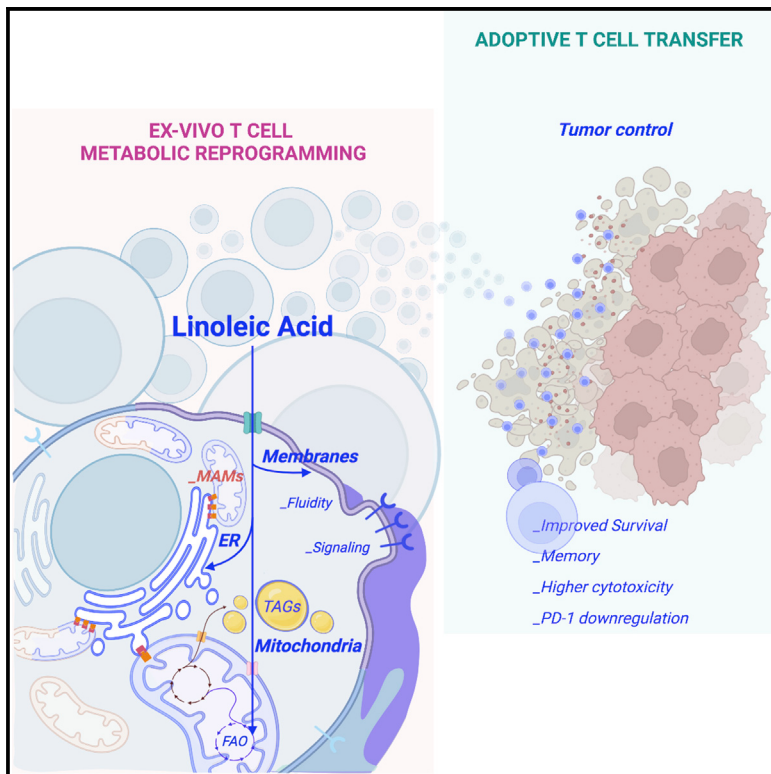


## Linoleic acid potentiates CD8<sup>+</sup> T cell metabolic fitness and antitumor immunity

### Graphical abstract



### Authors

Carina B. Nava Lauson, Silvia Tiberti,  
Paola A. Corsetto, ...,  
Simona Rodighiero, Luigi Nezi,  
Teresa Manzo

### Correspondence

teresa.manzo@ieo.it

### In brief

Nava-Lauson et al. report that linoleic acid potentiates antitumor function of CD8+ T cells by operating a profound metabolic reprogramming that protects from exhaustion and pushes toward a memory phenotype with superior cytotoxic functions. LA-redirected CD8+ T cells are empowered with an improved metabolic and functional fitness within the TME, thereby improving efficacy of ACT-based therapy.

### Highlights

- Linoleic acid (LA) improves “quality” and “quantity” of CTL mitochondria
- LA redirects CTL away from exhaustion and toward a memory-like phenotype
- LA fosters MERC formation and harnesses CTL with superior effector functions
- LA potentiates antitumor CTL response and improves ACT efficacy



## Article

# Linoleic acid potentiates CD8<sup>+</sup> T cell metabolic fitness and antitumor immunity

Carina B. Nava Lauson,<sup>1</sup> Silvia Tiberti,<sup>1</sup> Paola A. Corsetto,<sup>2</sup> Federica Conte,<sup>3</sup> Punit Tyagi,<sup>1</sup> Markus Machwirth,<sup>4</sup> Stefan Ebert,<sup>4</sup> Alessia Loffreda,<sup>5</sup> Lukas Scheller,<sup>6</sup> Dalia Sheta,<sup>6</sup> Zeinab Mokhtari,<sup>6</sup> Timo Peters,<sup>7,14</sup> Ayush T. Raman,<sup>8</sup> Francesco Greco,<sup>9,10</sup> Angela M. Rizzo,<sup>4</sup> Andreas Beilhack,<sup>6</sup> Giovanni Signore,<sup>9</sup> Nicola Tumino,<sup>11</sup> Paola Vacca,<sup>11</sup> Liam A. McDonnell,<sup>9</sup> Andrea Raimondi,<sup>5</sup> Philip D. Greenberg,<sup>12</sup> Johannes B. Huppa,<sup>7</sup> Simone Cardaci,<sup>13</sup> Ignazio Caruana,<sup>4</sup> Simona Rodighiero,<sup>1</sup> Luigi Nezi,<sup>1</sup> and Teresa Manzo<sup>1,15,\*</sup>

<sup>1</sup>Department of Experimental Oncology, Istituto Europeo di Oncologia IRCCS, Milano, Italy

<sup>2</sup>Department of Pharmacological and Biomolecular Sciences, University of Milan, Milan, Italy

<sup>3</sup>Institute for Systems Analysis and Computer Science "Antonio Ruberti," National Research Council, Rome, Italy

<sup>4</sup>Department of Paediatric Haematology, Oncology and Stem Cell Transplantation, University Hospital of Würzburg, Würzburg, Germany

<sup>5</sup>Experimental Imaging Center, IRCCS San Raffaele Scientific Institute, San Raffaele Vita-Salute University, Milano, Italy

<sup>6</sup>Interdisciplinary Center for Clinical Research (IZKF), Experimental Stem Cell Transplantation Laboratory, Würzburg University Hospital, Würzburg, Germany

<sup>7</sup>Medical University of Vienna, Center for Pathophysiology, Infectiology and Immunology, Institute for Hygiene and Applied Immunology, Vienna, Austria

<sup>8</sup>Broad Institute of MIT and Harvard, Cambridge, MA, USA

<sup>9</sup>Fondazione Pisana per la Scienza, ONLUS, San Giuliano Terme, Italy

<sup>10</sup>Institute of Life Sciences, Sant' Anna School of Advanced Studies, Pisa, Italy

<sup>11</sup>Immunology Research Area, Innate Lymphoid Cells Unit, Bambino Gesù Children's Hospital IRCCS, Rome, Italy

<sup>12</sup>Clinical Research Division and Program in Immunology, Fred Hutchinson Cancer Research Center, Seattle, WA, USA

<sup>13</sup>Division of Genetics and Cell Biology, IRCCS San Raffaele Scientific Institute, Milan, Italy

<sup>14</sup>Present address: LUMICKS, Paalbergweg 3, 1105 AG Amsterdam, the Netherlands

<sup>15</sup>Lead contact

\*Correspondence: teresa.manzo@ieo.it

<https://doi.org/10.1016/j.cmet.2023.02.013>

## SUMMARY

The metabolic state represents a major hurdle for an effective adoptive T cell therapy (ACT). Indeed, specific lipids can harm CD8<sup>+</sup> T cell (CTL) mitochondrial integrity, leading to defective antitumor responses. However, the extent to which lipids can affect the CTL functions and fate remains unexplored. Here, we show that linoleic acid (LA) is a major positive regulator of CTL activity by improving metabolic fitness, preventing exhaustion, and stimulating a memory-like phenotype with superior effector functions. We report that LA treatment enhances the formation of ER-mitochondria contacts (MERC), which in turn promotes calcium (Ca<sup>2+</sup>) signaling, mitochondrial energetics, and CTL effector functions. As a direct consequence, the antitumor potency of LA-instructed CD8 T cells is superior *in vitro* and *in vivo*. We thus propose LA treatment as an ACT potentiator in tumor therapy.

## INTRODUCTION

Adoptive T cell therapy (ACT) led to unparalleled clinical outcomes in the treatment of cancer,<sup>1–3</sup> but its efficacy—especially in solid tumors—is often limited by the scarce intratumor infiltration, persistence, and function of adoptively transferred T cells.<sup>4–7</sup>

Metabolic constraints imposed by the tumor microenvironment (TME) greatly influence the success of immune-based therapies.<sup>8–10</sup> The TME is indeed a complex and continuously evolving entity, where the type and availability of nutrients impact T cell functionality,<sup>11–13</sup> and depletion of essential nutrients and accumulation of toxic metabolic bioproducts in the TME can suppress antitumor responses, with lipid enrichment being frequently observed.<sup>10,14–17</sup> Different classes of lipids can act as metabolic intermediates, constituents of membranes, or

signaling molecules in immune cells, and several studies reported their influence on T cell proliferation, activation, and differentiation.<sup>18</sup> However, only specific long-chain fatty acids (LC-FAs) harm CD8<sup>+</sup> T cell (CTL) mitochondrial integrity and function, leading to exhaustion and defective antitumor immunity.<sup>14</sup> Whether all LC-FAs are detrimental to T cell functionality and how they regulate different CTL fate decisions have not been thoroughly investigated yet.

Among LC-FAs, linoleic acid (LA; C18:2n-6) is the most abundant ω-6 polyunsaturated fatty acid (PUFA)<sup>19</sup> assumed through diet,<sup>20</sup> with essential functions in health and disease.<sup>21</sup> However, its specific role on CTL immunity remains to be underscored, and in light of the impact of diet on immune function,<sup>22–24</sup> decoding its modulatory effect on CTL response might have important implications for cancer therapies.



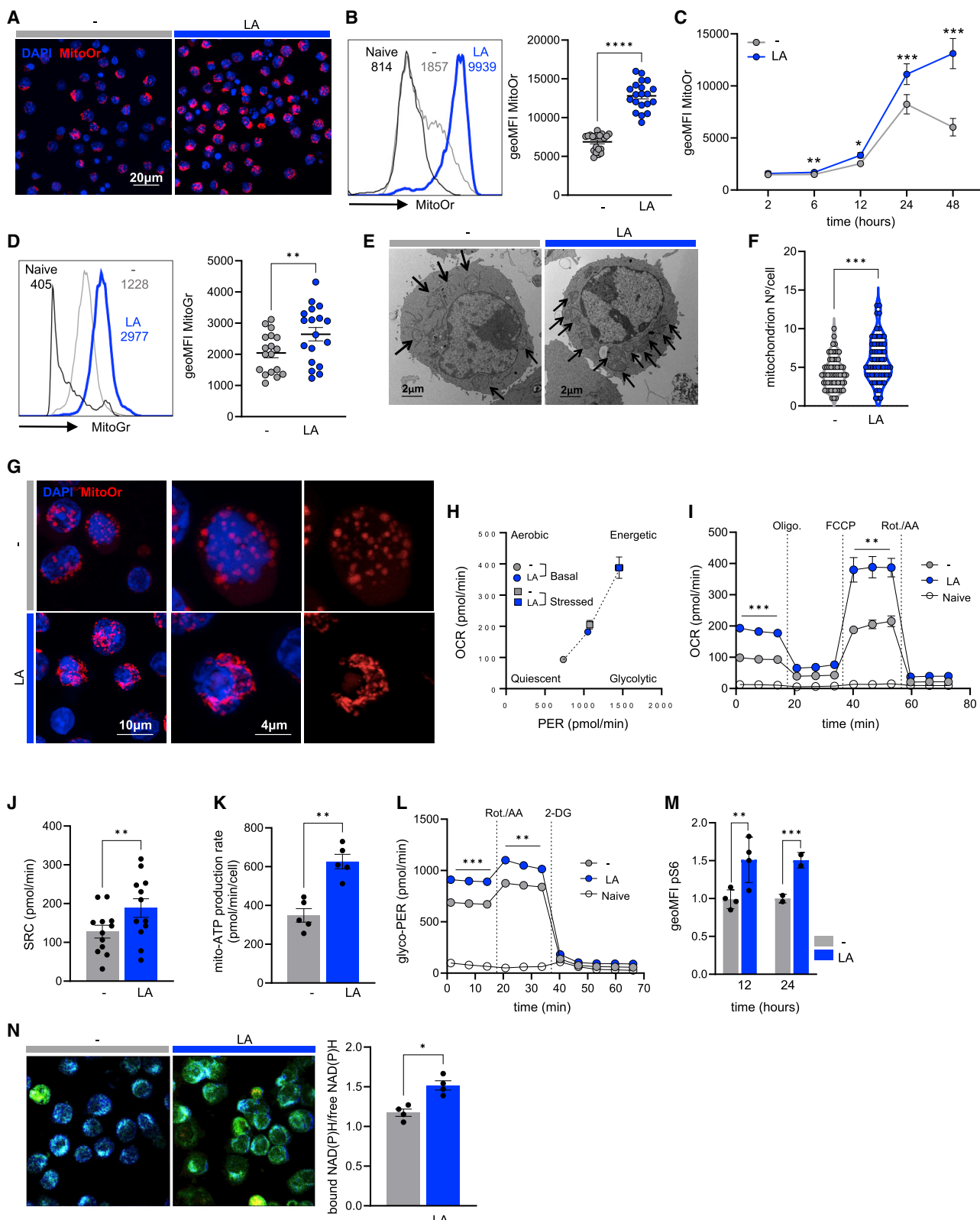


**Figure 1. LA enhances the quality and quantity of mitochondria in CTLs**

(A–C)  $\Delta\Psi_m$  assessed by immunofluorescence (A) and flow cytometry (B and C).

(D–F) Mitochondrial mass based on flow cytometry (D, n = 18/20; 4/5 independent experiments) and TEM (E and F, n = 3).

(legend continued on next page)

Here, we demonstrated that LA is a major positive regulator of CTL functionality by promoting mitochondrial fitness and a memory-like phenotype, which results in improved tumor control. Our findings lay the foundation for enhancing ACT efficacy and broadening its benefits to refractive malignancies through lipid-induced metabolic reprogramming of CTLs.

## RESULTS

### LA levels are modulated during T cell activation

LC-FAs are essential regulators of T cell activation, proliferation, and function.<sup>25,26</sup> We investigated whether different types of lipids regulate CTL responses by quantifying the composition and abundance of LC-FAs during T cell activation. When compared with naive CTLs, activated CTLs contained similar levels of SFAs (saturated FAs) but were different in terms of unsaturated FAs, with a significant decrease in PUFA (Figure S1A). In particular, the abundance of LA in CTLs was significantly lower on activation (Figure S1B), suggesting that it might be used or consumed during T cell activation. Thus, we decided to study the role of LA in tuning CTL fate and activity.

### LA enhances mitochondrial content and activity in CTLs

To decode whether LA has a role in regulating CTL metabolism, we measured mitochondrial content and function by activating CTLs in the presence of LA at a final concentration of 100 μM, in the range of plasma levels,<sup>25,27,28</sup> and compared them with controls (LA- versus CTR-CTLs).

We recorded a significant increase in mitochondrial membrane potential ( $\Delta\Psi_m$ ) on LA treatment (Figures 1A, 1B, and S1C), which did not affect CTL viability within the range of tested concentrations (Figure S1D). The rapid (within 6 h; Figure 1C) and long-lasting (Figure S1E) mitochondrial burst induced by LA was accompanied by an augmented mitochondrial content (Figures 1D–1F). Although LA-CTLs exhibited a significantly higher side scatter (SSC; Figure S1F), the observed mitochondrial effects were not due to changes in cell size (Figures S1G and S1H). Qualitatively, although CTR-CTLs were characterized by rounded mitochondria rather dispersed across the cytoplasm (Figure 1E, left panel), LA-CTLs exhibited rod-shaped and highly condensed mitochondria, mostly polarized at one edge of the cell (Figure 1E, right panel). These observations in LA-CTLs were corroborated by the elongated shape of mitochondria in LA-CTLs (Figure 1G), a distinctive sign of cells heavily relying on oxidative phosphorylation (OXPHOS).<sup>29</sup> Overall, these data indicate that LA upholds mitochondria quantity and quality in CTLs.

### LA reinforces CTL mitochondrial bioenergetics and metabolic fitness

Given the above findings, we postulated that LA might improve the CTL metabolic performance. Indeed, LA-CTL was more energetic under both resting and stressed conditions on an energetic map (Figure 1H), with a higher O<sub>2</sub> consumption rate

(OCR; Figures 1H, 1I, S1I, and S1J) and spare respiratory capacity (SRC; Figure 1J) in comparison to CTR-CTLs. Since etomoxir (Eto), a small molecule that inhibits fatty acid oxidation (FAO), overruled LA advantages on OCR (Figures S1K–S1M) and SRC (Figure S1N), we inferred that the improved ability of LA-CTLs to respond to stress conditions was FAO dependent. In accordance, LA-CTLs displayed increased levels of all components of the electron transport chain (ETC) and, in particular, complex V (ATP synthase; Figure S1O), which utilizes  $\Delta\Psi_m$  to generate ATP<sup>30</sup> that was indeed augmented in LA-CTLs (Figure 1K).

Alongside improved mitochondrial metabolism, LA-CTLs held a better glycolytic activity (Figures 1L, S1Q, and S1R), likely sustained by the upregulation of pS6 (Figure 1M), which in CTLs is essential for the execution of effector functions under stress.<sup>31</sup> However, the increase in the protein-bound NADH/free NADH ratios in fluorescence lifetime imaging microscopy (FLIM; Figure 1N) as well as higher OCR/extracellular acidification rate (ECAR) ratio (Figure S1S) highlighted that LA-CTLs preferentially use OXPHOS, in line with their increased mitochondrial content and activity. Notably, when tested on different tumor cell lines, LA was able to raise their  $\Delta\Psi_m$  (Figure S1T) but with variable effects on their bioenergetic profile (Figure S1U), postulating the existence of cell-type-specific LA-dependent wiring. Combined, these data suggest that LA endows CTLs with enhanced bioenergetics and metabolic fitness, likely making them more responsive to increased energetic demands and stressful conditions.

### LA improves CTL mitochondrial fitness and activity by promoting ER-mitochondria contacts

Next, to gain mechanistic insights into the LA effect on CTLs, we performed a transcriptional analysis of LA-CTLs compared with CTR-CTLs, which highlighted 1,970 differentially expressed genes (DEGs) (Figure S2A; Table S1). Gene ontology analysis highlighted the enrichment of pathways involved in lipid metabolism, mitochondria, ER and calcium homeostasis, and T cell receptor (TCR) signaling (Figure S2B–S2D).

To identify the groups of potential coregulated genes (modules, MEs), DEGs were first integrated with the most significant LA-induced effects using the Weighted Gene Co-expression Network Analysis (WGCNA; Table S2).<sup>32</sup> Focusing on the three MEs with the highest correlation score, genes in ME-1 (labeled in blue) were positively correlated with LA treatment, whereas those in ME-4 and ME-12 (labeled in brown and turquoise, respectively) showed a negative correlation (Figures 2A and S2E). Functional enrichment analysis confirmed the central involvement of mitochondria (i.e., mitochondrial inner membrane, mitochondrial matrix, and respiratory chain complex; Figure S2F), in agreement with the pivotal role of LA in boosting CTLs' mitochondrial activity.

On the other hand, LA regulated several ER-related transcripts<sup>33–38</sup> linked to its composition and structure (i.e. *Tmem147*, *Selenow*, *Cebpb*, *Bbc3*, and *Atf6*; Figures S3C and S3D), as well as genes of calcium influx regulation (such as

(G) Representative high-resolution confocal images obtained using 40× (left panels) and 100× (right panel).

(H–L) Metabolic profiling of CTL ± LA. Energetic map (H), OCR (I), SRC (J), mitochondrial-ATP production rate (K), and PER (L) based on Seahorse data. Plots are representative of 4 independent experiments.

(M) Phosphorylation of S6 by flow cytometry (n = 2/4; 2 independent experiments).

(N) NAD(P)H and free NAD(P)H assessed by FLIM (n = 4).

Data are represented as mean ± SEM. Paired (B–D and H–N) or unpaired (F) two-tailed Student's t test, \*p < 0.05, \*\*p < 0.01, \*\*\*p < 0.001, \*\*\*\*p < 0.0001.

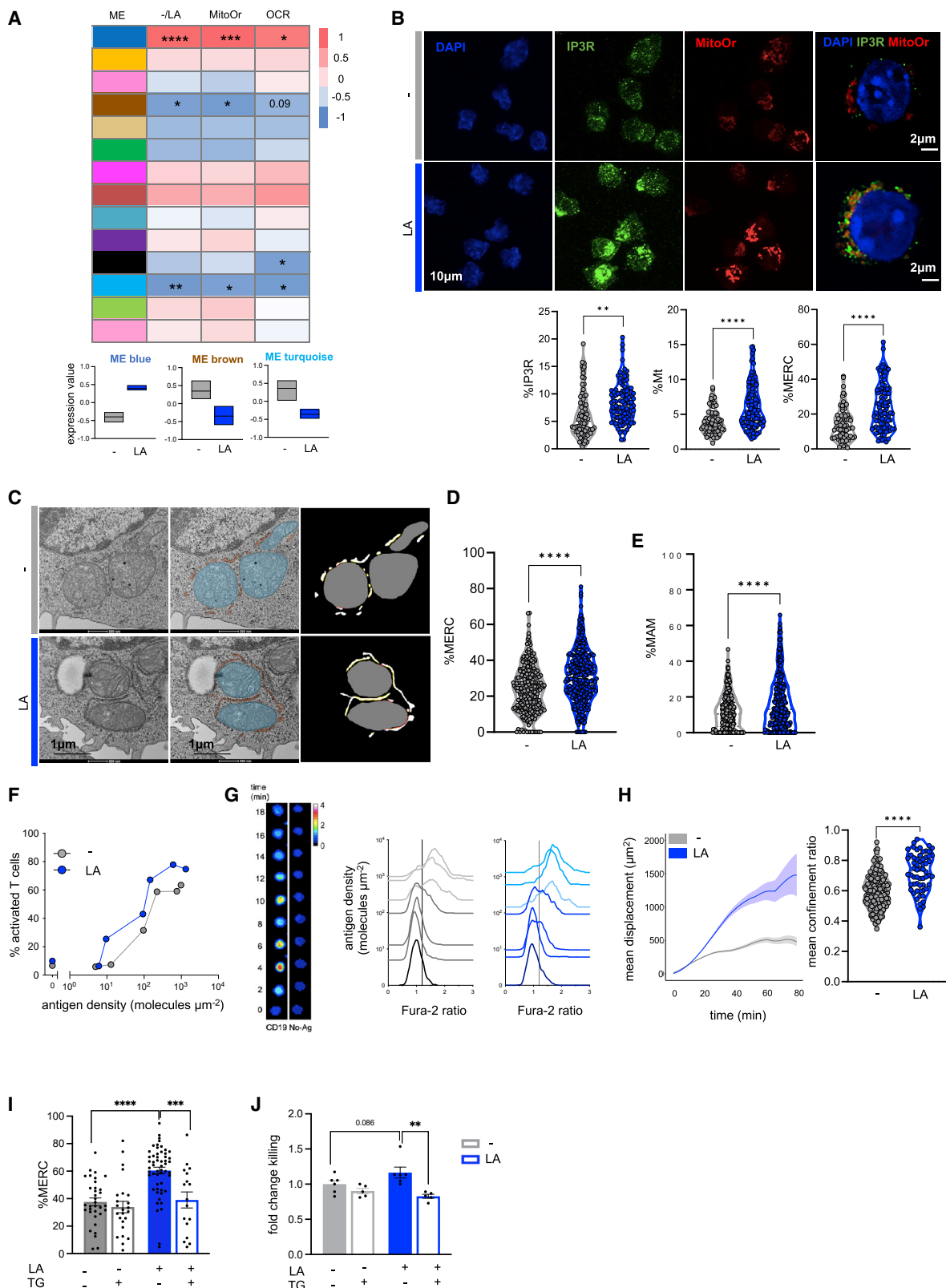


**Figure 2. LA improves CTL mitochondrial fitness and activity by promoting MAM formation**

(A) Heatmap from WGCNA. Each row corresponds to a module; each column to a trait of interest. The three modules exhibiting the higher p value are represented (bottom panel).

(legend continued on next page)

*Camk2g*, *Tmco6*, *Psen2*, and *Selenon*; Figures S2C–S2D), as instrumental to contain ER stress.<sup>39–42</sup>

These data suggested a tight co-regulation of mitochondrial fitness and ER homeostasis, in agreement with recent studies revealing that ER stress response controls T cell functionality by regulating mitochondrial activity.<sup>43,44</sup> Therefore, the paired involvement of the ER and mitochondria, in response to LA, was independently validated by quantifying the ER-resident Inositol 1,4,5-trisphosphate receptor type 1 ( $\alpha$ -IP3R1) while simultaneously monitoring mitochondria using MitoOr staining. The marked increase of both markers in LA-CTLs (Figure 2B) supported that LA regulated the mitochondria-ER network in CTLs.

Since mitochondria-ER contacts (MERCs) have been shown to modulate mitochondrial respiration in CTLs,<sup>45</sup> we investigated whether LA affects MERC formation in CTLs. Quantitative confocal microscopy (Figure 2B) and EM analysis (Figures 2C–2E) confirmed an increased frequency of MERCs (between 30 and 100 nm; Figure 2D) and mitochondrial-associated membranes (MAMs, below 30 nm; Figure 2E) in LA-CTLs, whereas fewer mitochondria were near the ER in CTR-CTLs.

MERCs are dynamic structures controlling the transport of  $\text{Ca}^{2+}$  from the ER to mitochondria<sup>46</sup> that are crucial for T cell activation, migration, and TCR signaling.<sup>47</sup> Accordingly, Fura-2-based time-lapsed calcium imaging demonstrated that LA-CTLs responded more vigorously and with increased sensitivity in antigen-limiting conditions, compared with CTR-CTLs (Figures 2F and 2G). Likewise, LA-CTLs migrated faster and further when compared with CTR-CTLs as assessed by increased confined migration (Figure 2H) and decreased turning angle (Figure S2G). In accordance, by disrupting  $\text{Ca}^{2+}$  homeostasis using thapsigargin (TG), an irreversible inhibitor of the sarco-endoplasmic reticulum  $\text{Ca}^{2+}$  ATPase (SERCA),<sup>46,48</sup> LA-CTLs showed a significant reduction in MERC formation (Figures 2I and S2H), mitochondrial activity (Figures S2H and S2I), and cytotoxic capacity (Figure 2J). Of note, TG did not influence the cytotoxic activity of CTR-CTLs (Figure 2J), which reflects the complexity of  $\text{Ca}^{2+}$  signaling in different T cell subsets. Overall, these results suggest that LA enhanced MERC formation and the downstream CTL processes associated with calcium signaling.

We next wondered whether LA integrates into the membranes of mitochondria, ER, and MERCs by assessing the lipid composition of their enriched subcellular fractions. The results indicate that LA indeed integrates into the organelle's subcellular fractions (Figure 3A) and modifies their lipid asset, inducing a drop of SFAs and MUFA and a prominent increase in PUFA abundance (Figure 3B), with the specific increase of PUFA n6 (Figure 3C) at the expenses of PUFA n3 (Figure 3D). Of note, the increase in PUFA n6 is entirely attributable to C18:2, since other PUFA n6 metabolites—such as C20:3 and C20:5—did not change (Figures 3E and 3F).

The increase of PUFA and consequently increased unsaturation levels in the membranes have been reported to positively regulate ER, mitochondria, and MAM functionality.<sup>49–51</sup> Accord-

ingly, we showed increased MERC formation (Figures 2B–2E), OXPHOS (Figures 1A–1C), and  $\text{Ca}^{2+}$  signaling (Figures 2F and 2G). Moreover, LA-CTL membranes displayed a high 18:2/16:0 ratio (Figure 3G), which indicates improved membrane fluidity. Thus, LA mediates a profound lipid remodeling of mitochondria, ER, and MERC membranes, thereby changing their chemical-physical properties and improving their functionality.

### LA-induced metabolic reprogramming redirects CTLs toward a memory phenotype with enhanced cytotoxic activity *in vitro*

Having found that LA promoted metabolic fitness and MERC formation, which are hallmarks of memory T cells,<sup>10,45,52</sup> we investigated whether LA also shapes CTL activation and differentiation. The t-distributed stochastic neighbor embedding (tSNE) analysis of multiparametric flow cytometry data identified three CTL clusters characterized by the highest  $\Delta\Psi\text{m}$  based on the calculated MitoOr MFI (Figure S3A) and specifically enriched in LA-CTLs and underrepresented in CTR-CTLs (Figure 4A).

The manual gating strategy revealed that LA-CTLs were predominantly CD44<sup>high</sup>/CD62L<sup>high</sup> memory cells, with low frequencies of CD44<sup>high</sup>/CD62L<sup>low</sup> effector cells (Figures 4B and S3B). In line with a skewing toward a memory phenotype, LA-CTL bears a higher expression of the canonical memory markers CD127 (Figure 4C) and CD62L (Figure S3C) and transcription factors Eomes (Figure 4D) and TCF1 (Figure 4E), both promoting a memory differentiation,<sup>53</sup> and low expression of the effector-associated marker Tbet (Figure S3D). Surprisingly, Blimp1, which is known to promote short-lived effector CTLs and favor exhaustion,<sup>54–56</sup> was significantly increased in LA-CTLs (Figure S3E). Nevertheless, LA-CTLs were predominantly defined by a CD127<sup>high</sup>/KLRG1<sup>low</sup> profile (Figure S3F), typical of long-lived memory cells and associated with an enhanced recall response.<sup>57</sup>

On the other side, LA-CTLs did not show any differences in proliferative capabilities (Figure S3G), expression of canonical activation markers (Figure S3H), or effector cytokines (i.e., GZM $\beta$ , IFN $\gamma$ , TNF $\alpha$ , IL2, and perforin; Figure S3I), confirming that LA did not influence CTL activation<sup>14</sup> but shaped their differentiation toward memory. Accordingly, LA-CTLs harbored a significant increase in cell number (Figure S3J), suggesting a survival advantage regarding CTR-CTLs (Figure S2B), and the capacity to simultaneously produce up to 5 effector cytokines, an ability known as T cell polyfunctionality and typical of memory CTLs (Figure 4F).

Strikingly, LA-CTLs showed a significant and sustained drop in PD1 expression on repeated cycles of stimulation (Figures 4G, 4H, and S3K), which was not due to a decreased activation status (Figures S3H and S3I). Concomitantly, the expression of TOX was diminished (Figure 4I), suggesting that LA reduced the likelihood to develop an exhausted phenotype.<sup>58–60</sup> Indeed, when evaluated for the ability to kill cognate antigen tumor cells, LA-CTLs were more efficient than CTR-CTLs, at the effector:target (E:T) ratio of 1:1 (Figures 4J and 4K), even on short exposure to

(B–E) MERC quantification by confocal microscopy (B) and TEM (C). ER-mitochondria contacts (distances between 100 and 30 nm, D) are shown in yellow, and ER-MAMs (distances  $\leq$  30 nm, E) are shown in red (right panels). n = 3.

(F and G)  $\text{Ca}^{2+}$  response and antigen sensitivity based on Fura-2 time-lapse microscopy.

(H) T cell migration assay and mean displacement ratio of CTL  $\pm$  LA.

(I and J) TG effect on MERC formation (I) and cytotoxic activity (J) after 12 h.

Data are represented as mean  $\pm$  SEM. Paired (I and J) or unpaired (B–H) two-tailed Student's t test, \*\*p < 0.01, \*\*\*p < 0.001, \*\*\*\*p < 0.0001.

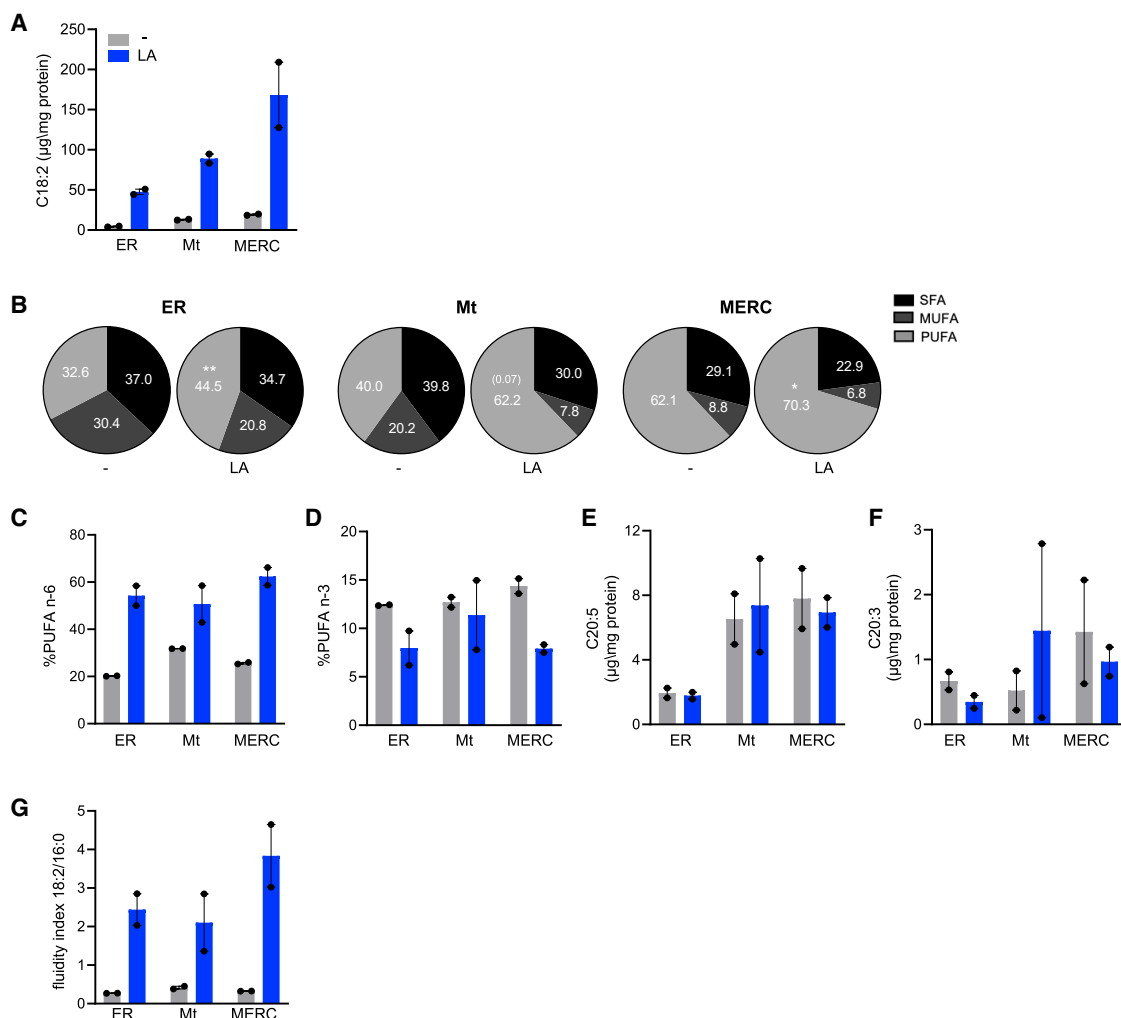


**Figure 3. LA remodels lipid composition of mitochondria, ER, and MERCs**

Lipidomics analysis on ER, mitochondria, and MERC fractions from CTL. Quantification of C18:2 (A); SFAs, MUFA, and PUFA (B); PUFA n6 (C); PUFA n3 (D); C20:5 (E); C20:3 (F); and fluidity index (G). n = 2.

LA (i.e., 12 h of LA; **Figure 4K**). Notably, their cytotoxic ability was maintained at the unfavorable E:T ratio of 1:4, when CTR-CTLs were no longer able to kill tumor cells (**Figures 4K** and **S3L**). Thus, we concluded that LA-induced metabolic reprogramming redirects CD8 T cells away from exhaustion and toward a memory phenotype with increased killing capacity.

Thereafter, we dissected the time sequence of the LA-induced phenotypes. LA, at first, induced a strong and quick modulation of ER within just 2 h (**Figure S4A**), followed at 6 h by the mitochondrial burst (**Figures 1C** and **S4B**), alongside MERC formation (**Figure S4C**). Since MERCs promote CTL functions,<sup>47,61</sup> the LA-induced modulation of the ER-mitochondria network resulted in an improved cytotoxic activity starting from 12 h (**Figure S4D**). Of note, by perturbing MERC or mitochondrial function (**Figure S4E**), the killing advantage of LA-CTLs was abrogated, confirming that LA integrates both mitochondrial and ER components to improve CTL response. The temporal gap between the increase in MitoOr and memory establishment (**Figures 1C**, **S4F**, and **S4G**), which appeared at 24 h, suggested that the memory shift is consequent to

the ER-mitochondria regulation operated by LA in CTLs. Thus, our data support a model in which LA, by promoting MERC formation, fosters mitochondrial metabolism and Ca<sup>2+</sup> signaling, which in concert promote cytotoxic activity, followed by improved metabolic fitness and skewing toward memory CTLs.

Interestingly, when we investigated how specific was the effect of LA on CTLs in comparison with other lipids (i.e., oleic acid [OA] and arachidonic acid [AA]) or glucose, known to modulate CTL responses,<sup>62,63</sup> we found that LA was unique in inducing the above-described metabolic and functional rewiring (**Figure S5**). Together, these data provide evidence that LA has a unique ability to foster a joint mitochondria-ER crosstalk in CTLs, which in turn regulates CTL fate and function.

#### LA regulates a metabolic program that stimulates lipid biosynthesis

To elucidate the metabolic program associated with LA treatment, we performed unbiased metabolomic profiling of LA- and CTR-CTLs. When compared with CTR-CTLs, LA-CTLs displayed

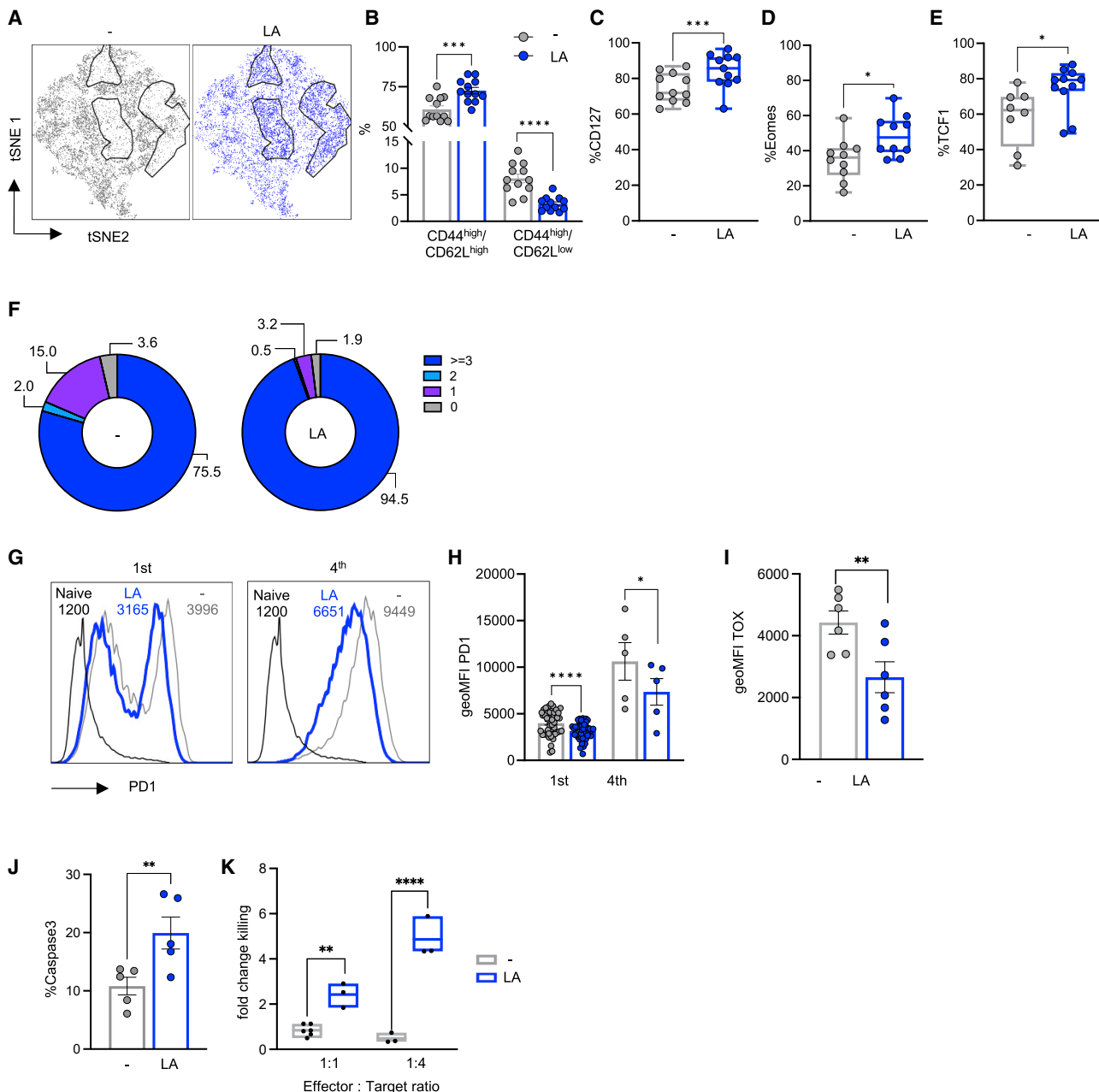


**Figure 4. LA-induced metabolic reprogramming redirects CTLs toward a memory-like phenotype with enhanced cytotoxic activity in vitro**

(A) tSNE representation based on  $\Delta\Psi m$  ( $n = 5$ ).

(B–E) Memory characterization measured as percentage of memory and effector cells (B); expression of CD127 (C), Eomes (D), and TCF1 (E) ( $n = 8/11$ ; 2–4 independent experiments).

(F) Effector cytokine polyfunctionality.

(G–I) Exhaustion profile assessed as PD1 (G and H,  $n = 15/5$ , 2 independent experiments) and TOX (I,  $n = 6$ ) expression levels.

(J and K) CTL killing capacity measured as caspase 3 (J,  $n = 5$ ; 2 independent experiments) and live staining (K,  $n = 6$ ; 2 independent experiments, fold change on CTR-CTL).

Data are represented as mean  $\pm$  SEM. Paired two-tailed Student's t test, \* $p < 0.05$ , \*\* $p < 0.01$ , \*\*\* $p < 0.001$ , \*\*\*\* $p < 0.0001$ .

differences in 49 metabolites (with  $p \leq 0.05$ , 43 upregulated and 3 downregulated; Figure S6A; Table S3). Surprisingly, LA- and CTRL-CTL showed the same abundance of most of the glycolytic and pentose phosphate pathway (PPP) intermediates and the same abundance of acetyl-CoA (Figures S6B–S6D).

On the other side, LA-CTLs showed increased expressions of glycolytic enzymes (*Hk*, *Hk2*, *PfkM*, *Aldo1*, and *Alco1*; Figure S2C) and a significant enrichment of fructose 1,6 bisphosphate (F16BP) (Figure S6A). These findings suggested that in LA-CTLs, the glycolytic intermediates rapidly diverted into the PPP,

likely to generate the reduced nicotinamide adenine dinucleotide phosphate (NADPH) needed for lipid biosynthesis.<sup>64</sup> In accordance, we registered an upregulation of several key enzymes in the PPP (*Ogdh*, *Tpi1*, *H6pd*, *Pgls*, *Tkt*, *Taldo1*, *Gls2*, *Cad*, and *Dhodh*; **Figure S2C**) crucial for reductive lipid biosynthesis as well as several other metabolic enzymes that promote NADPH generation (*Nadk*, *Mthfd*, *Aldh*, *Idh2*, and *Gsl2*; **Figure S2C**). NADPH is also used to maintain the intracellular redox balance, protecting cells against membrane lipid peroxidation and cell death,<sup>65</sup> in line with the increased levels of peroxidases (*Gpx*) and cysteinylglycine disulfide (GSSR; **Figure S6A**). Thus, we proposed here a model in which LA orchestrated glucose metabolism not as a mere energy-generating pathway but as a metabolic route to support the production of intermediates needed for FA synthesis.

In line with this model, we registered an upregulation of genes involved in FA synthesis (i.e., *Slc27a1*, *Aacs*, *Acaa2*, *Fasn*, *Srebf1*, *Cpt1a*, *Acadvl*, and *Slc25A1*; **Figure S2C**)<sup>66–68</sup> and mitochondrial citrate-malate antiport (*Slc25a1* or *Cic*)<sup>69</sup> that feed FA synthesis by transporting citrate from mitochondria to cytoplasm producing NADPH, and *Cpt1a*, which transports LC-FAs into mitochondria, thereby mediating FAO<sup>70</sup> (**Figures S2C** and **S2D**). Furthermore, LA-CTLs displayed a higher expression of key enzymes for triacylglyceride (TAG) synthesis (*Dgat2*), either from monoglycerol (*Mgat*) or G3P (*Agpat1-3*),<sup>71–73</sup> and their remodeling (*Mboat2* and *Mboat7*)<sup>74,75</sup> (**Figures S2C** and **S2D**). In conclusion, these data support a model in which LA orchestrates carbon metabolites toward FA synthesis. Accordingly, the most striking differences detected between LA- and CTR-CTLs were lipids related to LA, including long-chain polyunsaturated fatty acids (LC-PUFAs; i.e., tetradecadienoate, docosahexaenoate, linoleate, dihomo-linolenate, and docosadienoate), the monohydroxy fatty acid 13-hydroxyoctadecadienoic acid (13-HODE) derived from LA, and lineolyl-containing phosphatidyl- and lyso-phosphatidyl-cholines, ethanolamines, and sphingomyelins (**Figure S6A**). Moreover, we observed an increase in the levels of intermediates of glycerol metabolism, namely 1-linoleoylglycerol and 1-palmitoylglycerol (**Figure S6A**), which constitute the backbone of TAGs, known to regulate CTL fate.<sup>76</sup>

### LA induces profound lipid remodeling and storage in CTLs

Lipolysis of TAGs stored in lipid droplets (LDs) supplies FA for FAO in memory T cells.<sup>52</sup> Consistent with this scenario, LA-CTLs hold upregulation of LD-associated genes (*Bsc12*, *Lipe*, *Plin2*, *Hilpda*, and *Pnpla2*; **Figure S2C**), which stimulated an increase in LD formation (**Figure S6F**), suggesting that LA reroutes metabolism toward a futile cycle of simultaneous engagement of FAS (fatty acid synthesis) and FAO.<sup>77</sup>

Therefore, we employed <sup>13</sup>C-labeled LA to track its elongation, desaturation, and oxygenation<sup>78</sup> in CTLs. First, our data proved that LA was taken up by CTLs, as indicated by the accumulation of <sup>13</sup>C-LA in LA-CTLs regarding CTR-CTLs (**Figure 5A**), in accordance with the upregulation of *Slc27a1* (**Figures S2C** and **S2D**), an LC-FA transporter that facilitates LA import into CTLs.<sup>49,79,80</sup> It is worth noticing that we did not observe any changes in the expression of other proteins implicated in LC-FA uptake, including fatty acid translocase (CD36)<sup>81</sup> or fatty acid-binding proteins (FABPs).<sup>82</sup> LA was then metabolized in oxidized derivatives 9-

and 13-HODE, as indicated by the incorporations of <sup>13</sup>C-LA carbons in their own intracellular pool (**Figure 5B**). Moreover, <sup>13</sup>C-LA carbons are incorporated in LC-FAs, such as dihomolinoleate (C20:2 n-6; **Figure 5C**) and docosadienoate (C22:2 n-6; **Figure 5D**) levels, as well as more complex LA-derived lipids, such as 1,2-dilinoleoyl-GPC (18:2/18:2; **Figure 5E**) and 1-palmitoyl-2-linoleoyl-GPE (16:0/18:2; **Figure 5F**), suggesting that LA is incorporated and elongated into LC-FAs.

TAGs can then be used for membrane synthesis, directly influencing phospholipid (PL) remodeling.<sup>83</sup> In support of this notion, we observed the upregulation of genes implicated in the PL biosynthetic pathway (**Figures S2B–S2D**) and the incorporation of LA in PLs (**Figure S6A**). Moreover, LC-MS-based lipidomic analyses recorded broad changes in the abundance of several PLs (**Figure 5G**), especially phosphatidylcholines (PCs), phosphatidylethanolamines (PEs), lysophospholipids (LPLs), and sphingomyelins (SPHs). Notably, LA-CTLs displayed differences in the degree of saturation of LC-FAs, with a decreased abundance of saturated PLs, especially palmitoyl (16:0)-containing PLs (**Figure 5F**), in favor of polyunsaturated PLs, particularly linoleoyl (18:2)-containing PLs (**Figure 5E**). The increased fraction of unsaturated lipids is predicted to decrease membrane rigidity.<sup>84</sup> Indeed, the membranes were more fluid in LA-CTLs (**Figure 5I**), which might provide a mechanistic explanation of the reduced threshold for TCR clustering and activation in LA-CTLs (**Figures 2F** and **2G**), with the consequently improved cytotoxic activity (**Figures 4K** and **S3L**).

Taken together, these data indicate that although maximizing NADPH production sustains FAO and quenches reactive bio-products, LA diverts available resources toward the synthesis of TAGs, promoting PL remodeling by increasing unsaturation (**Figure 5J**). In doing so, LA changes the membrane fluidity, which ultimately endows CTLs with improved and sustained functionality.

### CTLs metabolically reprogrammed by LA carry out a superior antitumor response *in vivo*

To demonstrate that the *in vitro* LA-induced features were coupled with better fitness *in vivo*, we employed an ACT model for B16-OVA melanoma and OVA-specific T cells activated *ex vivo* in the presence or absence of LA (LA-ACT or ACT; **Figure 6A**).

LA-CTLs preserved their superior mitochondrial activity within the TME compared with CTR-CTLs (**Figure 6B**), confirming that LA-CTLs better coped with the metabolic constraints imposed by the TME. In line with their metabolic fitness, infiltrating LA-CTLs maintained an elevated expression of TCF1 (**Figure 6C**), which resulted in increased frequencies of CD44<sup>high</sup>/CD62L<sup>high</sup> cells in the LA-ACT group (**Figure 6D**). Of note, despite the expression of Blimp1 (**Figure S7A**), LA-CTLs maintained reduced KLRG1 levels (**Figure 6F**), suggesting that they are restrained from terminal differentiation even within the TME.<sup>85–87</sup> Remarkably, LA-CTLs were more resistant to exhaustion, as indicated by the lower frequencies of PD1<sup>+</sup> cells (**Figure 6G**) as well as PD1<sup>+</sup>TIM3<sup>+</sup> cells (**Figure 6H**). Likewise, LA-CTLs featured polyfunctionality within the TME (**Figure 6I**), whereas ≈40% of CTR-CTLs were no longer able to produce effector cytokines (**Figure 6I**). The advantages induced by LA treatment are specific to the TME and do not influence peripheral CTLs (**Figures S7B–S7E**). All these features enabled LA-ACT to control tumors more efficiently (**Figures 6J** and **S7F**), proving their superior

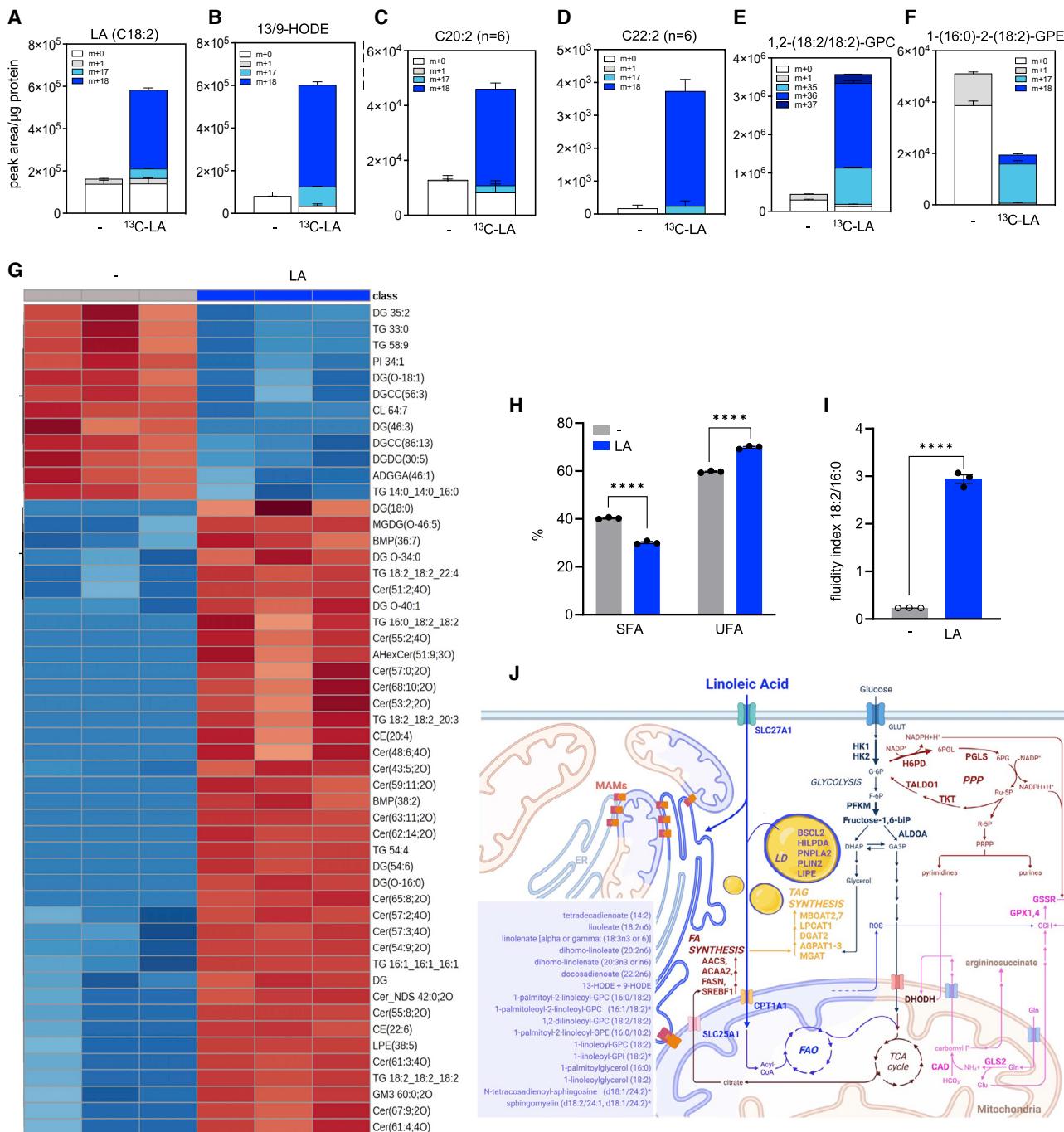


**Figure 5. LA induces a profound lipid remodeling in CTLs**

(A–F)  $^{13}\text{C}$ -labeled LA experiments ( $n = 2$ ). Quantification of C18:2 (A), 13/9-HODE (B), C20:2n6 (C), C22:2n6 (D), 1,2-(18:2/18:2)-GPC (E), and 1-(16:0)-2-(18:2)-GPE (F).

(G–I) LS-MS lipidomics ( $n = 3$ ). Heatmap (G), percentage of SFA and UFA (H), and fluidity index (I).

(J) Integrated view of metabolic and transcription changes induced by LA in CTLs.

Data are represented as mean  $\pm$  SEM. Paired two-tailed Student's t test, \*\*\* $p < 0.0001$ .

therapeutic potential. In conclusion, we have identified LA as an LC-FA able to induce profound metabolic reprogramming in CTLs that protects from exhaustion and pushes toward a memory phenotype with potent antitumor activity.

#### LA promotes mitochondrial activity and memory phenotype in human CTLs

To consolidate the therapeutic potential of the above findings, we first validated LA rewiring in human CTL *in vitro*. We

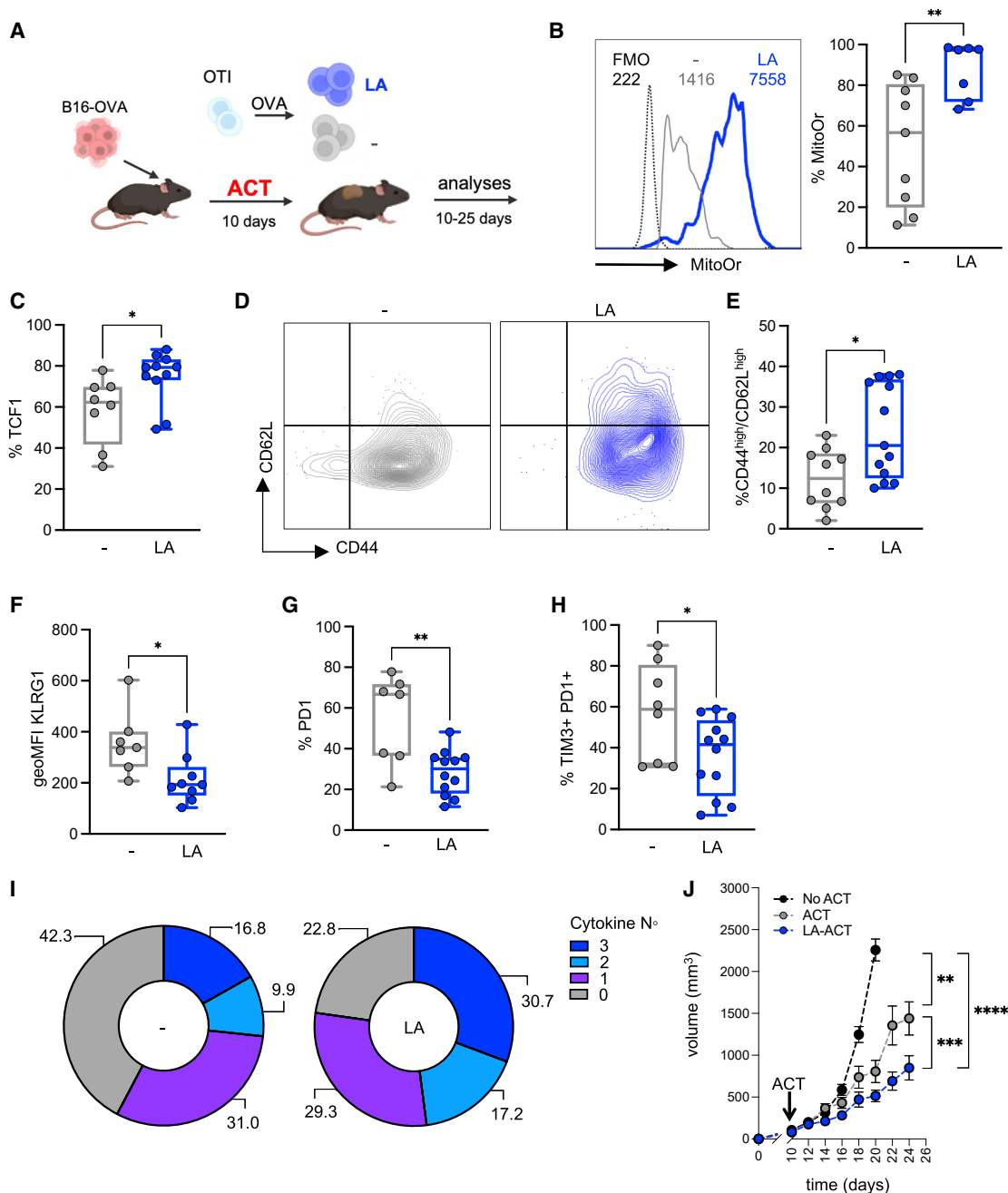


**Figure 6. LA-metabolically reprogrammed CTLs operate a superior antitumor response *in vivo***

(A) ACT experimental scheme.

(B–I) Analysis of the CTL infiltrate 14 days post-infusion. ΔΨm (B), memory phenotype—TCF1 (C), CD44<sup>high</sup>CD62L<sup>high</sup> (D and E), KLRG1 (F), exhaustion profile—PD1 (G), PD1+TIM3+ (H), and CTL polyfunctionality (I).

(J) Tumor growth curve ( $n = 20$  for ACT-LA, 20 for ACT, and 13 for No-ACT; 5 independent experiments).

Unpaired two-tailed Student's t test (B–H) or one-way ANOVA (J), \* $p < 0.05$ , \*\* $p < 0.01$ , \*\*\* $p < 0.001$ , \*\*\*\* $p < 0.0001$ .

confirmed an increase in ΔΨm (Figure S7G), leading to an overall enhanced energetic profile (Figures S7H–S7K) and central memory population (defined as CD62L<sup>+</sup>CD45RO<sup>+</sup>CD127<sup>+</sup>CD27<sup>+</sup> CTLs; Figure S7L), characterized by lower PD1 expression (Figure S7M). Thus, similar to what we observed in mice, LA also shapes metabolic fitness and fate in human CTLs.

### LA improves CAR-T cell therapy efficacy

In view of the promising benefits induced by LA on CTLs, we validated LA treatment as a new strategy to improve ACT efficacy. Thus, we applied *ex vivo* LA treatment on a clinically relevant system that employs human chimeric antigen receptor T (CAR-T) cells. Here, we have assayed the performance of three different

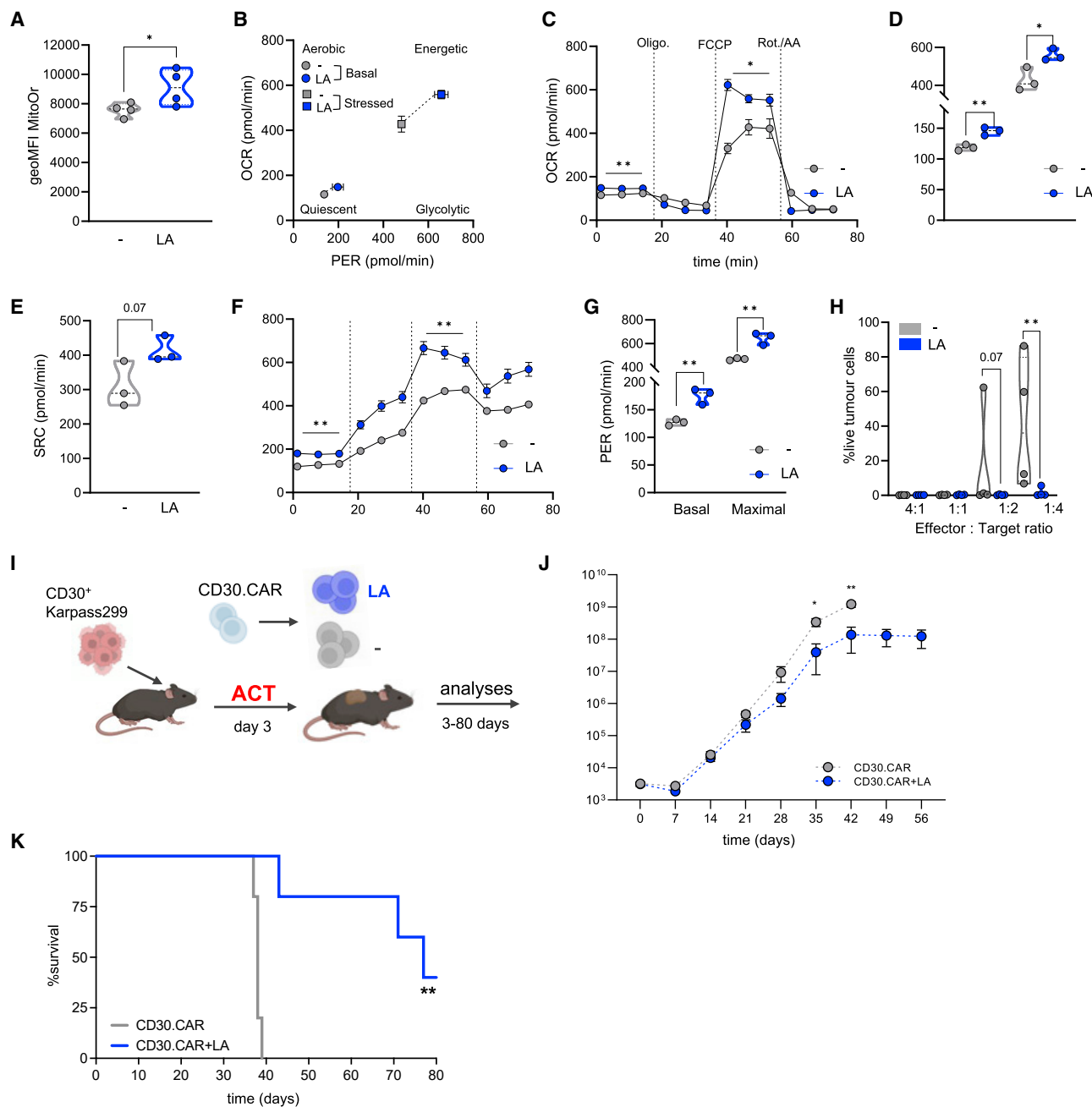


**Figure 7. LA improves CAR-T cell therapy efficacy**

(A)  $\Delta\Psi_m$  staining in CD30.CAR-T cells.

(B–G) Metabolic profile of CD30.CAR-T cells: energetic map (B), OCR (C and D), SRC (E), and PER (F and G).

(H) *In vitro* cytotoxic assay ( $n = 6$ ; 2 independent experiments).

(I) ACT experiment with CD30.CAR T cells.

(J and K) Tumor progression (J) and Kaplan-Meier curve (K) ( $n = 5$ ).

Data are represented as mean  $\pm$  SEM. Paired (A–G) or unpaired (H–K) two-tailed Student's t test, \* $p < 0.05$ , \*\* $p < 0.01$ .

LA redirected CAR-T cells: CD30.CAR-T (for non-Hodgkin and lymphoma),<sup>88</sup> GD2.CAR-T (for neuroblastoma, some high-grade glioma, and sarcoma),<sup>89</sup> and CD19.CAR-T (for acute lymphoblastic leukemia and diffuse large B cell lymphoma).<sup>90</sup>

In accordance with the data presented above, on LA treatment, we found a significant increase in  $\Delta\Psi_m$ , independently

of the CAR construct tested (Figures 7A, S7N, and S7O). Accordingly, LA-treated CAR-T cells uphold their highly energetic metabolic profile (Figures 7B–7G). Thus, LA promoted higher metabolic fitness in CAR-T cells. Next, we tested our CAR-T on a long-term co-culture assay with target tumor cells. Both LA-treated and control CAR-T cells show efficient killing when

cultured at an E:T ratio of 1:1 with tumor cells (Figures 7H, S7P, and S7Q). However, only LA-treated CAR-T cells retain cytotoxic capabilities when incubated with higher proportions of tumor cells (1:2 and 1:4; Figures 7H, S7P, and S7Q), suggesting that LA enhances CAR-T cell functions.

Finally, we tested the tumor control ability of LA-redirected CAR-T cells *in vivo* by employing a CD30.CAR ACT model for lymphoma<sup>88</sup> (Figure 7I). In line with previous findings, non-treated CD30.CAR-T cells fail to control tumor burden, and all mice were euthanized by day 35. By contrast, LA-CAR-T cells efficiently controlled tumors (Figures 7J and S7R) and promoted long-term survival (4/5 survive up to day 80; Figure 7K). In conclusion, LA-ACT affords long-lasting tumor control and long-term survival.

In summary, LA can all at once overcome several obstacles encountered by CTLs within the TME. Thus, our data identify LA as a tool to endow CTLs with increased metabolic fitness and tumor response and provide initial evidence of the therapeutic relevance of this approach.

## DISCUSSION

The TME dampens the ability of CTLs to execute antitumor immunity.<sup>91</sup> Nutrient availability and metabolic crosstalk have been shown to affect CTL fate in the TME,<sup>26,92,93</sup> with lipids emerging as key drivers.<sup>94</sup> Their accumulation is a hallmark of different types of tumors<sup>14,16,17,24,95,96</sup> where they are associated with CTL dysfunction. However, the specific effects of different LC-FAs on CTL biology have not yet been fully understood. In particular, PUFAs have an immunomodulatory effect also on CTLs,<sup>18,97</sup> but their mechanisms remain quite controversial. Our study reveals that LA, an essential PUFA, ameliorates CTL function and memory differentiation through mitochondrial reprogramming, ultimately preventing CTL exhaustion and granting improved antitumor responses.

LA was unique in operating a coordinated regulation of mitochondria and ER, which resulted in improved CTL metabolic fitness and functionality, implying that different FAs modulate CTL fate and function, each by inducing a peculiar metabolic change. Deciphering the specific mechanisms behind the different lipid-induced CTL control would be crucial to decode their influence on antitumor immunity. On the other hand, our data paint an even more complex scenario, which includes cell-type-specific sensing mechanisms for lipids. Indeed, LA has been previously shown to cause cell death in CD4 T cells,<sup>98</sup> where utilization of FAO correlates with PD1 expression.<sup>99</sup> By contrast, here, we showed that LA did not affect cellular viability, and it modulated  $\Delta\Psi_m$  of CTLs and tumor cell lines with cell-specific effects on their energetic profile. Thus, we postulated that different lipids may be instrumental to achieve cell-specific modulation of mitochondrial metabolism and, as a consequence, cell functionality.

Our data indicate that lipids can be used to coordinate the CTL-mediated antitumor responses through the modulation of mitochondrial function. Emphasis has been laid on mitochondrial plasticity in regulating CTL fate and function,<sup>70,100–102</sup> preventing T cell exhaustion,<sup>103–108</sup> and promoting the generation of memory T cells.<sup>52,76,109</sup> However, the uncertainty surrounding the molecular circuits coordinating metabolic state and cellular functions has so far prevented an effective targeted manipulation.

Here, we show that LA is able to promote memory formation while simultaneously maintaining effector and cytotoxic functions in CTLs by integrating mitochondrial respiration with glucose metabolism, which likely endows them with sustained functionality in the TME. The elevated glycolytic capacity in LA-instructed CTLs provides the intermediates necessary to fuel anabolic reactions in CTLs,<sup>64</sup> which are essential to support their superior effector functions.<sup>110,111</sup> In this regard, the use of a futile cycle coupling FA synthesis with FAO<sup>52</sup> couples with LD generation as a mechanism to store lipids and protect CTLs from lipotoxicity during high lipid burden.<sup>112,113</sup> Although this model may sound wasteful from an energetic perspective, it would ensure memory CTLs a higher overall metabolic fitness for a quicker response in the event of re-stimulation.<sup>110</sup> Our results further develop this concept by highlighting the influence that LA has on the membrane's lipid composition and saturation. Indeed, the resulting increase in membrane fluidity induced by LA concurs to improve CTL sensitivity to antigens and results in superior cytotoxic activity. Further studies will be necessary to better understand how LA-mediated biophysical changes differentially affect signaling pathways in TME-exposed CTLs.

LA-induced metabolic and functional reprogramming is dependent on MERC formation, likely because favoring transmission of  $\text{Ca}^{2+}$  signals between ER and mitochondria<sup>114</sup> potentiates CTL function.<sup>115</sup> Interestingly, our data suggest that the impact of  $\text{Ca}^{2+}$  signaling perturbation might be influenced by T cell identity and vary across different T cell subsets. Whether changes in  $\text{Ca}^{2+}$  signaling levels activate different transcriptional and metabolic programs awaits future investigations. It would be interesting to dissect the mechanisms of calcium sensitivity in relation to CTL fate and metabolic requirements.

ACT is hampered by the acquisition of a dysfunctional state in CTLs, which impairs their function and persistence within the TME. Infused T cells quickly lose their metabolic plasticity, critical to adapt to a highly immunosuppressive TME. Recent findings have underscored the importance of metabolic programs in T cell survival and effector function.<sup>116–119</sup> Considering the current roadblocks, our findings offer a tangible potential for LA treatment to turn ACT into a clinical success, regardless of the initial fitness of the T cell product. Indeed, LA skewed CTLs toward a memory-like phenotype, preventing their terminal differentiation and exhaustion while retaining high effector activities. In this regard, the finding of Blimp1 upregulation was of interest and raises the possibility that it might have a role in establishing effector functions in LA-driven memory CTLs. However, it remained to decode the mechanism by which LA could link Blimp1 and metabolic regulation for the acquisition of effector functions in memory CTLs.

LA significantly improves antitumor responses toward several tumor types, including multiple myeloma and lymphoma, and even when targeting solid tumors such as melanoma and neuroblastoma. In this scenario, it is conceivable to believe that metabolic pathways taken by CTLs, in relation to the nutrients they consume, direct them toward different effector profiles, and targeted manipulation of such *modus operandi* might lead to advances in T cell-based therapies. Of considerable benefit, our approach concerns *ex vivo* treatment of isolated T cells and is not limited by any need to target the lipid metabolism systematically that would otherwise risk adverse side effects.<sup>120–123</sup> Last, but not the least, LA treatment confers long-lasting

metabolic and functional advantages to T cells, which are maintained inside the TME. In all, LA is able to ameliorate ACT efficacy and to broaden its application for the treatment of a wide range of malignancies.

Taken together, our results show that lipids have a major effect on T cell physiology, engaging different metabolic, functional, and cellular programs. Based on our study, we envision that lipids will become integral to tailoring T cell-mediated immune responses in immune-based cancer therapy.

### Limitations of study

In this work, we identified LA as a potent enhancer of CTL responses on promoting a metabolic reprogramming, which grants functional fitness and tumor control. Modulations induced by LA affect CTLs at the transcriptional, metabolic, and biophysical levels. However, which is the individual contribution of each of these changes to CTL metabolic reprogramming, functional fitness, and tumor control remains to be addressed. Furthermore, the molecular reasons behind the unique advantages provided by LA in comparison to other lipids remain unexplored. Finally, the LA-induced metabolic reprogramming was only studied in the context of CTLs; future work is required to understand its effects in other cellular contexts, such as CD4 T cells, myeloid cells, and different tumor types. These studies may also inform about benefits and side effects related to diet intervention as an approach to improve the efficacy of cancer therapy.

### STAR★METHODS

Detailed methods are provided in the online version of this paper and include the following:

- KEY RESOURCES TABLE

- RESOURCE AVAILABILITY

- Lead contact
  - Materials availability
  - Data and code availability

- EXPERIMENTAL MODEL AND SUBJECT DETAILS

- METHOD DETAILS

- CD8<sup>+</sup> T cell isolation and activation
  - Immunophenotype and flow cytometry
  - tSNE analysis
  - Immunofluorescence and confocal microscopy
  - Time-lapse microscopy
  - Fluorescence lifetime imaging microscopy (FLIM)
  - Metabolic assays
  - Electron microscopy
  - MAM's and ER-mitochondria contact's analysis
  - RNA-seq and analysis
  - Calcium influx
  - Metabolomics and lipidomic assays
  - Total cell lysate preparation and cell fractionation
  - Immunoblots
  - Lactate assay
  - Acetyl Co-A assay
  - Adoptive cell transfer (ACT) experiments
  - Isolation and culture of primary human T lymphocytes
  - CAR-T cell engineering and GMP protocols

- QUANTIFICATION AND STATISTICAL ANALYSIS

### SUPPLEMENTAL INFORMATION

Supplemental information can be found online at <https://doi.org/10.1016/j.cmet.2023.02.013>.

### ACKNOWLEDGMENTS

We thank all members of T.M. and L.N. laboratories for discussion and experimental support; Eros Lazzerini Denchi and Ivan Marazzi for useful discussion of the manuscript; the Genomic Unit, Imaging Unit, and Flow Cytometry at IEO for their technical assistance; ALEMBIC (Advanced Light and Electron Microscopy BiolImaging Center) at IRCCS Ospedale San Raffaele for EM analyses; and Giulia Casorati and Paolo Dellabona for providing the B16-OVA cell line. This work was supported by the Associazione Italiana per la Ricerca contro il Cancro (AIRC StartUp grant 20464 to S.C., AIRC IG 26406 to L.N., and AIRC StartUp grant 21474 to T.M.), Bando della Ricerca Finalizzata 2018 GR-2018-12365954 to S.C., Deutsche Forschungsgemeinschaft (no. 470198222) and DKMS Stiftung Leben Spenden – John Hansen Research Grant (no. DKMS-SLS-JHRG-2021-03) to I.C., and DFG TRR221 Z02 (no. 324392634) to A.B. C.B.N.L., and S.T. are PhD students within the European School of Molecular Medicine (SEMM). This work was partially supported by the Italian Ministry of Health with Ricerca Corrente and 5x1000 funds. C.B.N.L. dedicates this work to José-Gregorio Nava. T.M. thanks Leonardo and Lara Nezi for their continuous support.

### AUTHOR CONTRIBUTIONS

C.B.N.L. and T.M. design the study. C.B.N.L., S.T., P.A.C., M.M., S.E., L.S., D.S., T.P., F.G., N.T., and P.V. performed the experiments; C.B.N.L., S.T., P.A.C., F.C., Z.M., P.T., A.L., A.T.R., T.P., A.R., J.B.H., S.C., I.C., S.R., L.N., and T.M. analyzed the data; A.B., G.S., L.A.M., P.D.G., J.B.H., S.C., and I.C. provided critical expertise and resources; C.B.N.L., S.T., L.N., and T.M. wrote and edited the manuscript; and T.M. coordinated the whole study. All the authors discussed and read the manuscript.

### DECLARATION OF INTERESTS

C.B.N.L., L.N., and T.M. reported a patent application related to this study. P.D.G. was a scientific consultant for Juno Therapeutics.

### INCLUSION AND DIVERSITY

One or more of the authors of this paper self-identifies as an underrepresented ethnic minority in their field of research or within their geographical location. One or more of the authors of this paper self-identifies as a member of the LGBTQIA+ community.

Received: June 9, 2022

Revised: December 19, 2022

Accepted: February 15, 2023

Published: March 9, 2023

### REFERENCES

1. Rosenberg, S.A., and Restifo, N.P. (2015). Adoptive cell transfer as personalized immunotherapy for human cancer. *Science* 348, 62–68. <https://doi.org/10.1126/science.aaa4967>.
2. Finck, A.V., Blanchard, T., Roselle, C.P., Golinelli, G., and June, C.H. (2022). Engineered cellular immunotherapies in cancer and beyond. *Nat. Med.* 28, 678–689. <https://doi.org/10.1038/s41591-022-01765-8>.
3. Brown, C.E., and Mackall, C.L. (2019). CAR T cell therapy: inroads to response and resistance. *Nat. Rev. Immunol.* 19, 73–74. <https://doi.org/10.1038/s41577-018-0119-y>.
4. Leon, E., Ranganathan, R., and Savoldo, B. (2020). Adoptive T cell therapy: boosting the immune system to fight cancer. *Semin. Immunol.* 49, 101437. <https://doi.org/10.1016/j.smim.2020.101437>.

5. Mondino, A., and Manzo, T. (2020). To remember or to forget: the role of good and bad memories in adoptive T cell therapy for tumors. *Front. Immunol.* 11, 1915. <https://doi.org/10.3389/fimmu.2020.01915>.
6. Good, C.R., Aznar, M.A., Kuramitsu, S., Samareh, P., Agarwal, S., Donahue, G., Ishiyama, K., Wellhausen, N., Rennels, A.K., Ma, Y., et al. (2021). An NK-like CAR T cell transition in CAR T cell dysfunction. *Cell* 184, 6081–6100.e26. <https://doi.org/10.1016/j.cell.2021.11.016>.
7. Larson, R.C., and Maus, M.V. (2021). Recent advances and discoveries in the mechanisms and functions of CAR T cells. *Nat. Rev. Cancer* 21, 145–161. <https://doi.org/10.1038/s41568-020-00323-z>.
8. Kishton, R.J., Sukumar, M., and Restifo, N.P. (2017). Metabolic regulation of T cell longevity and function in tumor immunotherapy. *Cell Metab.* 26, 94–109. <https://doi.org/10.1016/j.cmet.2017.06.016>.
9. DePeaux, K., and Delgoffe, G.M. (2021). Metabolic barriers to cancer immunotherapy. *Nat. Rev. Immunol.* 21, 785–797. <https://doi.org/10.1038/s41577-021-00541-y>.
10. Li, W., and Zhang, L. (2020). Rewiring mitochondrial metabolism for CD8+ T cell memory formation and effective cancer immunotherapy. *Front. Immunol.* 11, 1834. <https://doi.org/10.3389/fimmu.2020.01834>.
11. Elia, I., and Haigis, M.C. (2021). Metabolites and the tumour microenvironment: from cellular mechanisms to systemic metabolism. *Nat. Metab.* 3, 21–32. <https://doi.org/10.1038/s42255-020-00317-z>.
12. Scharping, N.E., Menk, A.V.v., Moreci, R.S., Whetstone, R.D., Dadey, R.E., Watkins, S.C., Ferris, R.L., and Delgoffe, G.M. (2016). The tumor microenvironment represses T cell mitochondrial biogenesis to drive intratumoral T cell metabolic insufficiency and dysfunction. *Immunity* 45, 374–388. <https://doi.org/10.1016/j.immuni.2016.07.009>.
13. Tumino, N., Nava Lauson, C.B., Tiberti, S., Besi, F., Martini, S., Fiore, P.F., Scodamaglia, F., Mingari, M.C., Moretta, L., Manzo, T., et al. (2023). The tumor microenvironment drives NK cell metabolic dysfunction leading to impaired antitumor activity. *Int. J. Cancer* 152, 1698–1706. <https://doi.org/10.1002/ijc.34389>.
14. Manzo, T., Prentice, B.M., Anderson, K.G., Raman, A., Schalck, A., Codreanu, G.S., Nava Lauson, C.B., Tiberti, S., Raimondi, A., Jones, M.A., et al. (2020). Accumulation of long-chain fatty acids in the tumor microenvironment drives dysfunction in intrapancreatic CD8+ T cells. *J. Exp. Med.* 217, e20191920. <https://doi.org/10.1084/jem.20191920>.
15. Xu, S., Chaudhary, O., Rodríguez-Morales, P., Sun, X., Chen, D., Zappasodi, R., Xu, Z., Pinto, A.F.M., Williams, A., Schulze, I., et al. (2021). Uptake of oxidized lipids by the scavenger receptor CD36 promotes lipid peroxidation and dysfunction in CD8+ T cells in tumors. *Immunity* 54, 1561–1577.e7. <https://doi.org/10.1016/j.immuni.2021.05.003>.
16. Ma, X., Bi, E., Lu, Y., Su, P., Huang, C., Liu, L., Wang, Q., Yang, M., Kalady, M.F., Qian, J., et al. (2019). Cholesterol induces CD8+ T cell exhaustion in the tumor microenvironment. *Cell Metab.* 30, 143–156.e5. <https://doi.org/10.1016/j.cmet.2019.04.002>.
17. Su, P., Wang, Q., Bi, E., Ma, X., Liu, L., Yang, M., Qian, J., and Yi, Q. (2020). Enhanced lipid accumulation and metabolism are required for the differentiation and activation of tumor-associated macrophages. *Cancer Res.* 80, 1438–1450. <https://doi.org/10.1158/0008-5472.CAN-19-2994>.
18. Howie, D., ten Bokum, A., Necula, A.S., Cobbold, S.P., and Waldmann, H. (2017). The role of lipid metabolism in T lymphocyte differentiation and survival. *Front. Immunol.* 8, 1949. <https://doi.org/10.3389/fimmu.2017.01949>.
19. Hamilton, J.S., and Klett, E.L. (2021). Linoleic acid and the regulation of glucose homeostasis: a review of the evidence. *Prostaglandins Leukot. Essent. Fatty Acids* 175, 102366. <https://doi.org/10.1016/j.plefa.2021.102366>.
20. Whelan, J., and Fritzsche, K. (2013). Linoleic acid. *Adv. Nutr.* 4, 311–312. <https://doi.org/10.3945/an.113.003772>.
21. Belury, M.A. (2002). Dietary conjugated linoleic acid in health: physiological effects and mechanisms of action. *Annu. Rev. Nutr.* 22, 505–531. <https://doi.org/10.1146/annurev.nutr.22.021302.121842>.
22. Salvadori, G., Zanardi, F., Iannelli, F., Lobefaro, R., Vernieri, C., and Longo, V.D. (2021). Fasting-mimicking diet blocks triple-negative breast cancer and cancer stem cell escape. *Cell Metab.* 33, 2247–2259.e6. <https://doi.org/10.1016/j.cmet.2021.10.008>.
23. Spencer, C.N., McQuade, J.L., Gopalakrishnan, V., McCulloch, J.A., Vetzou, M., Cogdill, A.P., Khan, M.A.W., Zhang, X., White, M.G., Peterson, C.B., et al. (2021). Dietary fiber and probiotics influence the gut microbiome and melanoma immunotherapy response. *Science* 374, 1632–1640. <https://doi.org/10.1126/science.aaz7015>.
24. Dyck, L., Prendeville, H., Raverdeau, M., Wilk, M.M., Loftus, R.M., Douglas, A., McCormack, J., Moran, B., Wilkinson, M., Mills, E.L., et al. (2022). Correction: suppressive effects of the obese tumor microenvironment on CD8 T cell infiltration and effector function. *J. Exp. Med.* 219, e20210042. <https://doi.org/10.1084/jem.20210042>.
25. Mauro, C., Smith, J., Cucchi, D., Coe, D., Fu, H., Bonacina, F., Baragetti, A., Cermenati, G., Caruso, D., Mitro, N., et al. (2017). Obesity-induced metabolic stress leads to biased effector memory CD4+ T cell differentiation via PI3K p110δ-Akt-mediated signals. *Cell Metab.* 25, 593–609. <https://doi.org/10.1016/j.cmet.2017.01.008>.
26. Chapman, N.M., Boothby, M.R., and Chi, H. (2020). Metabolic coordination of T cell quiescence and activation. *Nat. Rev. Immunol.* 20, 55–70. <https://doi.org/10.1038/s41577-019-0203-y>.
27. Abdelmagid, S.A., Clarke, S.E., Nielsen, D.E., Badawi, A., El-Sohemy, A., Mutch, D.M., and Ma, D.W.L. (2015). Comprehensive profiling of plasma fatty acid concentrations in young healthy Canadian adults. *PLoS One* 10, e0116195. <https://doi.org/10.1371/journal.pone.0116195>.
28. Terpstra, A.H. (2004). Effect of conjugated linoleic acid on body composition and plasma lipids in humans: an overview of the literature. *Am. J. Clin. Nutr.* 79, 352–361. <https://doi.org/10.1093/ajcn/79.3.352>.
29. Youle, R.J., and van der Bliek, A.M. (2012). Mitochondrial fission, fusion, and stress. *Science* 337, 1062–1065. <https://doi.org/10.1126/science.1219855>.
30. Yin, M., and O'Neill, L.A.J. (2021). The role of the electron transport chain in immunity. *FASEB J.* 35, e21974. <https://doi.org/10.1096/fj.202101161R>.
31. Finlay, D.K., Rosenzweig, E., Sinclair, L.V., Feijoo-Carnero, C., Hukelmann, J.L., Rolf, J., Panteleyev, A.A., Okkenhaug, K., and Cantrell, D.A. (2012). PDK1 regulation of mTOR and hypoxia-inducible factor 1 integrate metabolism and migration of CD8+ T cells. *J. Exp. Med.* 209, 2441–2453. <https://doi.org/10.1084/jem.20112607>.
32. Langfelder, P., and Horvath, S. (2008). WGCNA: an R package for weighted correlation network analysis. *BMC Bioinformatics* 9, 559. <https://doi.org/10.1186/1471-2105-9-559>.
33. Signal, E., Blangy, A., Martin, M., Gauthier-Rouvière, C., and Fort, P. (2001). Kinectin is a key effector of RhoG microtubule-dependent cellular activity. *Mol. Cell. Biol.* 21, 8022–8034. <https://doi.org/10.1128/MCB.21.23.8022-8034.2001>.
34. Wang, N., Clark, L.D., Gao, Y., Kozlov, M.M., Shemesh, T., and Rapoport, T.A. (2021). Mechanism of membrane-curvature generation by ER-tubule shaping proteins. *Nat. Commun.* 12, 568. <https://doi.org/10.1038/s41467-020-20625-y>.
35. Christodoulou, A., Maimiris, G., Makrigiorgi, A., Charidemou, E., Lüchtenborg, C., Verteris, A., Georgiou, R., Lederer, C.W., Haffner, C., Brügger, B., et al. (2020). TMEM147 interacts with lamin B receptor, regulates its localization and levels, and affects cholesterol homeostasis. *J. Cell Sci.* 133, jcs245357. <https://doi.org/10.1242/jcs.245357>.
36. Shen, Z.Q., Huang, Y.L., Teng, Y.C., Wang, T.W., Kao, C.H., Yeh, C.H., and Tsai, T.F. (2021). CISD2 maintains cellular homeostasis. *Biochim. Biophys. Acta Mol. Cell. Res.* 1868, 118954. <https://doi.org/10.1016/j.bbamcr.2021.118954>.
37. Bian, C., Marchetti, A., Hammel, P., and Cosson, P. (2021). Intracellular targeting of Cisd2/Miner1 to the endoplasmic reticulum. *BMC Mol. Cell Biol.* 22, 48. <https://doi.org/10.1186/s12860-021-00387-1>.

38. Parashar, S., and Ferro-Novick, S. (2022). Architecture of the endoplasmic reticulum plays a role in proteostasis. *Autophagy* 18, 937–938. <https://doi.org/10.1080/15548627.2022.2030175>.
39. Pitts, M.W., and Hoffmann, P.R. (2018). Endoplasmic reticulum-resident selenoproteins as regulators of calcium signaling and homeostasis. *Cell Calcium* 70, 76–86. <https://doi.org/10.1016/j.ceca.2017.05.001>.
40. Zampese, E., Fasolato, C., Kipanyula, M.J., Bortolozzi, M., Pozzan, T., and Pizzo, P. (2011). Presenilin 2 modulates endoplasmic reticulum (ER)-mitochondria interactions and Ca<sup>2+</sup> cross-talk. *Proc. Natl. Acad. Sci. USA* 108, 2777–2782. <https://doi.org/10.1073/pnas.1100735108>.
41. Ozcan, L., Cristina de Souza, J., Harari, A.A., Backs, J., Olson, E.N., and Tabas, I. (2013). Activation of calcium/calmodulin-dependent protein kinase II in obesity mediates suppression of hepatic insulin signaling. *Cell Metab.* 18, 803–815. <https://doi.org/10.1016/j.cmet.2013.10.011>.
42. Krebs, J., Agellon, L.B., and Michalak, M. (2015). Ca(2+) homeostasis and endoplasmic reticulum (ER) stress: an integrated view of calcium signaling. *Biochem. Biophys. Res. Commun.* 460, 114–121. <https://doi.org/10.1016/j.bbrc.2015.02.004>.
43. Cao, Y., Trillo-Tinoco, J., Sierra, R.A., Anadon, C., Dai, W., Mohamed, E., Cen, L., Costich, T.L., Magliocco, A., Marchion, D., et al. (2019). ER stress-induced mediator C/EBP homologous protein thwarts effector T cell activity in tumors through T-bet repression. *Nat. Commun.* 10, 1280. <https://doi.org/10.1038/s41467-019-09263-1>.
44. Cubillos-Ruiz, J.R., Silberman, P.C., Rutkowski, M.R., Chopra, S., Perales-Puchalt, A., Song, M., Zhang, S., Bettigole, S.E., Gupta, D., Holcomb, K., et al. (2015). ER stress sensor XBP1 controls anti-tumor immunity by disrupting dendritic cell homeostasis. *Cell* 161, 1527–1538. <https://doi.org/10.1016/j.cell.2015.05.025>.
45. Bantug, G.R., Fischer, M., Grählert, J., Balmer, M.L., Unterstab, G., Develioglu, L., Steiner, R., Zhang, L., Costa, A.S.H., Gubser, P.M., et al. (2018). Mitochondria-endoplasmic reticulum contact sites function as immunometabolic hubs that orchestrate the rapid recall response of memory CD8+ T cells. *Immunity* 48, 542–555.e6. <https://doi.org/10.1016/j.immuni.2018.02.012>.
46. Masud, A., Mohapatra, A., Lakhani, S.A., Ferrandino, A., Hakem, R., and Flavell, R.A. (2007). Endoplasmic reticulum stress-induced death of mouse embryonic fibroblasts requires the intrinsic pathway of apoptosis. *J. Biol. Chem.* 282, 14132–14139. <https://doi.org/10.1074/jbc.M700077200>.
47. Missiroli, S., Paternani, S., Caroccia, N., Pedriali, G., Perrone, M., Previati, M., Wieckowski, M.R., and Giorgi, C. (2018). Mitochondria-associated membranes (MAMs) and inflammation. *Cell Death Dis.* 9, 329. <https://doi.org/10.1038/s41419-017-0027-2>.
48. Iurlaro, R., and Muñoz-Pinedo, C. (2016). Cell death induced by endoplasmic reticulum stress. *FEBS Journal* 283, 2640–2652. <https://doi.org/10.1111/febs.13598>.
49. Lee, S.M., Lee, S.H., Jung, Y., Lee, Y., Yoon, J.H., Choi, J.Y., Hwang, C.Y., Son, Y.H., Park, S.S., Hwang, G.S., et al. (2020). FABP3-mediated membrane lipid saturation alters fluidity and induces ER stress in skeletal muscle with aging. *Nat. Commun.* 11, 5661. <https://doi.org/10.1038/s41467-020-19501-6>.
50. Renne, M.F., Bao, X., Hokken, M.W., Bierhuizen, A.S., Hermansson, M., Sprenger, R.R., Ewing, T.A., Ma, X., Cox, R.C., Brouwers, J.F., et al. (2022). Molecular species selectivity of lipid transport creates a mitochondrial sink for di-unsaturated phospholipids. *EMBO J.* 41, e106837. <https://doi.org/10.1525/embj.2020106837>.
51. Roman, I., Gmaj, P., Nowicka, C., and Angielski, S. (1979). Regulation of Ca<sup>2+</sup> efflux from kidney and liver mitochondria by unsaturated fatty acids and Na<sup>+</sup> ions. *Eur. J. Biochem.* 102, 615–623. <https://doi.org/10.1111/j.1432-1033.1979.tb04279.x>.
52. O'Sullivan, D., van der Windt, G.J., Huang, S.C.C., Curtis, J.D., Chang, C.H., Buck, M.D.L., Qiu, J., Smith, A.M., Lam, W.Y., DiPlato, L.M., et al. (2014). Memory CD8(+) T cells use cell-intrinsic lipolysis to support the metabolic programming necessary for development. *Immunity* 41, 75–88. <https://doi.org/10.1016/j.immuni.2014.06.005>.
53. Doering, T.A., Crawford, A., Angelosanto, J.M., Paley, M.A., Ziegler, C.G., and Wherry, E.J. (2012). Network analysis reveals centrally connected genes and pathways involved in CD8+ T cell exhaustion versus memory. *Immunity* 37, 1130–1144. <https://doi.org/10.1016/j.immuni.2012.08.021>.
54. Welsh, R.M. (2009). Blimp hovers over T cell immunity. *Immunity* 31, 178–180. <https://doi.org/10.1016/j.immuni.2009.08.005>.
55. Rutishauser, R.L., Martins, G.A., Kalachikov, S., Chandele, A., Parish, I.A., Meffre, E., Jacob, J., Calame, K., and Kaech, S.M. (2009). Transcriptional repressor Blimp-1 promotes CD8(+) T cell terminal differentiation and represses the acquisition of central memory T cell properties. *Immunity* 31, 296–308. <https://doi.org/10.1016/j.immuni.2009.05.014>.
56. Kallies, A., Xin, A., Belz, G.T., and Nutt, S.L. (2009). Blimp-1 transcription factor is required for the differentiation of effector CD8(+) T cells and memory responses. *Immunity* 31, 283–295. <https://doi.org/10.1016/j.immuni.2009.06.021>.
57. Parish, I.A., and Kaech, S.M. (2009). Diversity in CD8(+) T cell differentiation. *Curr. Opin. Immunol.* 21, 291–297. <https://doi.org/10.1016/j.co.2009.05.008>.
58. Scott, A.C., Dündar, F., Zumbo, P., Chandran, S.S., Klebanoff, C.A., Shakiba, M., Trivedi, P., Menocal, L., Appleby, H., Camara, S., et al. (2019). TOX is a critical regulator of tumour-specific T cell differentiation. *Nature* 571, 270–274. <https://doi.org/10.1038/s41586-019-1324-y>.
59. Alfei, F., Kanev, K., Hofmann, M., Wu, M., Ghoneim, H.E., Roelli, P., Utzschneider, D.T., von Hoesslin, M., Cullen, J.G., Fan, Y., et al. (2019). TOX reinforces the phenotype and longevity of exhausted T cells in chronic viral infection. *Nature* 571, 265–269. <https://doi.org/10.1038/s41586-019-1326-9>.
60. Khan, O., Giles, J.R., McDonald, S., Manne, S., Ngiow, S.F., Patel, K.P., Werner, M.T., Huang, A.C., Alexander, K.A., Wu, J.E., et al. (2019). TOX transcriptionally and epigenetically programs CD8+ T cell exhaustion. *Nature* 571, 211–218. <https://doi.org/10.1038/s41586-019-1325-x>.
61. Perrone, M., Caroccia, N., Genovese, I., Missiroli, S., Modesti, L., Pedriali, G., Vezzani, B., Vitto, V.A.M., Antenori, M., Lebiedzinska-Arciszewska, M., et al. (2020). The role of mitochondria-associated membranes in cellular homeostasis and diseases. *Int. Rev. Cell Mol. Biol.* 350, 119–196. <https://doi.org/10.1016/bs.ircmb.2019.11.002>.
62. Liao, P., Wang, W., Wang, W., Kryczek, I., Li, X., Bian, Y., Sell, A., Wei, S., Grove, S., Johnson, J.K., et al. (2022). CD8+ T cells and fatty acids orchestrate tumor ferroptosis and immunity via ACSL4. *Cancer Cell* 40, 365–378.e6. <https://doi.org/10.1016/j.ccr.2022.02.003>.
63. Carrillo, C., Hichami, A., Andreoletti, P., Cherkoui-Malki, M., del Mar Cavia, M., Abdoul-Azize, S., Alonso-Torre, S.R., and Khan, N.A. (2012). Diacylglycerol-containing oleic acid induces increases in [Ca<sup>2+</sup>(i)] via TRPC3/6 channels in human T-cells. *Biochim. Biophys. Acta* 1821, 618–626. <https://doi.org/10.1016/j.bbapap.2012.01.008>.
64. Vander Heiden, M.G.V., Cantley, L.C., and Thompson, C.B. (2009). Understanding the Warburg effect: the metabolic requirements of cell proliferation. *Science* 324, 1029–1033. <https://doi.org/10.1126/science.1160809>.
65. Aquilano, K., Baldelli, S., and Cirio, M.R. (2014). Glutathione: new roles in redox signalling for an old antioxidant. *Front. Pharmacol.* 5, 196.
66. Hume, D.A., and Weidemann, M.J. (1979). Role and regulation of glucose metabolism in proliferating cells. *J. Natl. Cancer Inst.* 62, 3–8. <https://doi.org/10.1093/jnci/62.1.3>.
67. DeBerardinis, R.J., Mancuso, A., Daikhin, E., Nissim, I., Yudkoff, M., Wehrli, S., and Thompson, C.B. (2007). Beyond aerobic glycolysis: transformed cells can engage in glutamine metabolism that exceeds the requirement for protein and nucleotide synthesis. *Proc. Natl. Acad. Sci. USA* 104, 19345–19350. <https://doi.org/10.1073/pnas.1007947104>.
68. Lunt, S.Y., and vander Heiden, M.G. (2011). Aerobic glycolysis: meeting the metabolic requirements of cell proliferation. *Annu. Rev. Cell Dev. Biol.* 27, 441–464. <https://doi.org/10.1146/annurev-cellbio-092910-154237>.
69. Catalina-Rodriguez, O., Kolukula, V.K., Tomita, Y., Preet, A., Palmieri, F., Wellstein, A., Byers, S., Giaccia, A.J., Glasgow, E., Albanese, C., et al.

- (2012). The mitochondrial citrate transporter, CIC, is essential for mitochondrial homeostasis. *Oncotarget* 3, 1220–1235. <https://doi.org/10.18632/oncotarget.714>.
70. Buck, M.D., O'Sullivan, D., Klein Geltink, R.I., Curtis, J.D., Chang, C.H., Sanin, D.E., Qiu, J., Kretz, O., Braas, D., van der Windt, G.J.W., et al. (2016). Mitochondrial dynamics controls T cell fate through metabolic programming. *Cell* 166, 63–76. <https://doi.org/10.1016/j.cell.2016.05.035>.
  71. Gijón, M.A., Riekhof, W.R., Zarini, S., Murphy, R.C., and Voelker, D.R. (2008). Lysophospholipid acyltransferases and arachidonate recycling in human neutrophils. *J. Biol. Chem.* 283, 30235–30245. <https://doi.org/10.1074/jbc.M806194200>.
  72. Matsuda, S., Inoue, T., Lee, H.C., Kono, N., Tanaka, F., Gengyo-Ando, K., Mitani, S., and Arai, H. (2008). Member of the membrane-bound O-acyltransferase (MBOAT) family encodes a lysophospholipid acyltransferase with broad substrate specificity. *Genes Cells* 13, 879–888. <https://doi.org/10.1111/j.1365-2443.2008.01212.x>.
  73. Zhao, Y., Chen, Y.Q., Bonacci, T.M., Bredt, D.S., Li, S., Bensch, W.R., Moller, D.E., Kowala, M., Konrad, R.J., and Cao, G. (2008). Identification and characterization of a major liver lysophosphatidylcholine acyltransferase. *J. Biol. Chem.* 283, 8258–8265. <https://doi.org/10.1074/jbc.M710422200>.
  74. Moessinger, C., Klizaite, K., Steinhagen, A., Philippou-Massier, J., Shevchenko, A., Hoch, M., Ejsing, C.S., and Thiele, C. (2014). Two different pathways of phosphatidylcholine synthesis, the Kennedy Pathway and the Lands Cycle, differentially regulate cellular triacylglycerol storage. *BMC Cell Biol.* 15, 43. <https://doi.org/10.1186/s12860-014-0043-3>.
  75. Mancina, R.M., Dongiovanni, P., Petta, S., Pingitore, P., Meroni, M., Rametta, R., Borén, J., Montalcini, T., Pujia, A., Wiklund, O., et al. (2016). The MBOAT7-TMC4 variant rs641738 increases risk of nonalcoholic fatty liver disease in individuals of European descent. *Gastroenterology* 150, 1219–1230.e6. <https://doi.org/10.1053/j.gastro.2016.01.032>.
  76. Cui, G., Staron, M.M., Gray, S.M., Ho, P.C., Amezquita, R.A., Wu, J., and Kaech, S.M. (2015). IL-7-induced glycerol transport and TAG synthesis promotes memory CD8+ T cell longevity. *Cell* 161, 750–761. <https://doi.org/10.1016/j.cell.2015.03.021>.
  77. Almeida, L., Lochner, M., Berod, L., and Sparwasser, T. (2016). Metabolic pathways in T cell activation and lineage differentiation. *Semin. Immunol.* 28, 514–524. <https://doi.org/10.1016/j.smim.2016.10.009>.
  78. Astarita, G., Kendall, A.C., Dennis, E.A., and Nicolaou, A. (2015). Targeted lipidomic strategies for oxygenated metabolites of polyunsaturated fatty acids. *Biochim. Biophys. Acta* 1857, 456–468. <https://doi.org/10.1016/j.bbapap.2014.11.012>.
  79. Lee, C.H., Olson, P., Hevener, A., Mehl, I., Chong, L.W., Olefsky, J.M., Gonzalez, F.J., Ham, J., Kang, H., Peters, J.M., et al. (2006). PPAR $\delta$  regulates glucose metabolism and insulin sensitivity. *Proc. Natl. Acad. Sci. USA* 103, 3444–3449. <https://doi.org/10.1073/pnas.0511253103>.
  80. Stahl, A., Hirsch, D.J., Gimeno, R.E., Punreddy, S., Ge, P., Watson, N., Patel, S., Kotler, M., Raimondi, A., Tartaglia, L.A., et al. (1999). Identification of the major intestinal fatty acid transport protein. *Mol. Cell* 4, 299–308. [https://doi.org/10.1016/S1097-2765\(00\)80332-9](https://doi.org/10.1016/S1097-2765(00)80332-9).
  81. Coburn, C.T., Knapp, F.F., Febbraio, M., Beets, A.L., Silverstein, R.L., and Abumrad, N.A. (2000). Defective uptake and utilization of long chain fatty acids in muscle and adipose tissues of CD36 knockout mice. *J. Biol. Chem.* 275, 32523–32529. <https://doi.org/10.1074/jbc.M003826200>.
  82. Nieman, K.M., Kenny, H.A., Penicka, C.V., Ladanyi, A., Buell-Gutbrod, R., Zillhardt, M.R., Romero, I.L., Carey, M.S., Mills, G.B., Hotamisligil, G.S., et al. (2011). Adipocytes promote ovarian cancer metastasis and provide energy for rapid tumor growth. *Nat. Med.* 17, 1498–1503. <https://doi.org/10.1038/nm.2492>.
  83. Currie, E., Schulze, A., Zechner, R., Walther, T.C., and Farese, R.V. (2013). Cellular fatty acid metabolism and cancer. *Cell Metab.* 18, 153–161. <https://doi.org/10.1016/j.cmet.2013.05.017>.
  84. Hac-Wydro, K., and Wydro, P. (2007). The influence of fatty acids on model cholesterol/phospholipid membranes. *Chem. Phys. Lipids* 150, 66–81. <https://doi.org/10.1016/j.chemphyslip.2007.06.213>.
  85. Hendler-Brandstetter, D., Ishigame, H., Shinnakasu, R., Plajer, V., Stecher, C., Zhao, J., Lietzenmayer, M., Kroehling, L., Takumi, A., Kometani, K., et al. (2018). KLRLG1+ effector CD8+ T cells lose KLRLG1, differentiate into all memory T cell lineages, and convey enhanced protective immunity. *Immunity* 48, 716–729.e8. <https://doi.org/10.1016/j.immun.2018.03.015>.
  86. Kaech, S.M., Tan, J.T., Wherry, E.J., Konieczny, B.T., Surh, C.D., and Ahmed, R. (2003). Selective expression of the interleukin 7 receptor identifies effector CD8 T cells that give rise to long-lived memory cells. *Nat. Immunol.* 4, 1191–1198. <https://doi.org/10.1038/ni1009>.
  87. Schluns, K.S., Kieper, W.C., Jameson, S.C., and Lefrançois, L. (2000). Interleukin-7 mediates the homeostasis of naïve and memory CD8 T cells in vivo. *Nat. Immunol.* 1, 426–432. <https://doi.org/10.1038/80868>.
  88. Guercio, M., Orlando, D., Cecca di, S., Sinibaldi, M., Boffa, I., Caruso, S., Abbaszadeh, Z., Camera, A., Cembrola, B., Bovetti, K., et al. (2021). CD28.OX40 co-stimulatory combination is associated with long in vivo persistence and high activity of CAR.CD30 T-cells. *Haematologica* 106, 987–999. <https://doi.org/10.3324/haematol.2019.231183>.
  89. Tumino, N., Weber, G., Besi, F., del Bufalo, F., Bertaina, V., Paci, P., Quattrini, L., Antonucci, L., Sinibaldi, M., Quintarelli, C., et al. (2021). Polymorphonuclear myeloid-derived suppressor cells impair the anti-tumor efficacy of GD2.CAR T-cells in patients with neuroblastoma. *J. Hematol. Oncol.* 14, 191. <https://doi.org/10.1186/s13045-021-01193-0>.
  90. Fraietta, J.A., Lacey, S.F., Orlando, E.J., Pruteanu-Malinici, I., Gohil, M., Lundh, S., Boesteanu, A.C., Wang, Y., O'Connor, R.S., Hwang, W.T., et al. (2018). Determinants of response and resistance to CD19 chimeric antigen receptor (CAR) T cell therapy of chronic lymphocytic leukemia. *Nat. Med.* 24, 563–571. <https://doi.org/10.1038/s41591-018-0010-1>.
  91. Anderson, K.G., Stromnes, I.M., and Greenberg, P.D. (2017). Obstacles posed by the tumor microenvironment to T cell activity: a case for synergistic therapies. *Cancer Cell* 31, 311–325. <https://doi.org/10.1016/j.ccr.2017.02.008>.
  92. Chapman, N.M., and Chi, H. (2022). Metabolic adaptation of lymphocytes in immunity and disease. *Immunity* 55, 14–30. <https://doi.org/10.1016/j.immuni.2021.12.012>.
  93. Bader, J.E., Voss, K., and Rathmell, J.C. (2020). Targeting metabolism to improve the tumor microenvironment for cancer immunotherapy. *Mol. Cell* 78, 1019–1033. <https://doi.org/10.1016/j.molcel.2020.05.034>.
  94. Lim, S.A., Su, W., Chapman, N.M., and Chi, H. (2022). Lipid metabolism in T cell signaling and function. *Nat. Chem. Biol.* 18, 470–481. <https://doi.org/10.1038/s41589-022-01017-3>.
  95. Herber, D.L., Cao, W., Nefedova, Y., Novitskiy, S.V., Nagaraj, S., Tyurin, V.A., Corzo, A., Cho, H.I., Celis, E., Lennox, B., et al. (2010). Lipid accumulation and dendritic cell dysfunction in cancer. *Nat. Med.* 16, 880–886. <https://doi.org/10.1038/nm.2172>.
  96. Veglia, F., Tyurin, V.A., Blasi, M., de Leo, A., Kossenkov, A.V., Dontireddy, L., To, T.K.J., Schug, Z., Basu, S., Wang, F., et al. (2019). Fatty acid transport protein 2 reprograms neutrophils in cancer. *Nature* 569, 73–78. <https://doi.org/10.1038/s41586-019-1118-2>.
  97. Zurier, R.B. (1993). Fatty acids, inflammation and immune responses. *Prostaglandins Leukot. Essent. Fatty Acids* 48, 57–62. [https://doi.org/10.1016/0952-3278\(93\)90010-T](https://doi.org/10.1016/0952-3278(93)90010-T).
  98. Ma, C., Kesarwala, A.H., Eggert, T., Medina-Echeverz, J., Kleiner, D.E., Jin, P., Stroncek, D.F., Terabe, M., Kapoor, V., ElGindi, M., et al. (2016). NAFLD causes selective CD4(+) T lymphocyte loss and promotes hepatocarcinogenesis. *Nature* 531, 253–257. <https://doi.org/10.1038/nature16969>.
  99. Patoukis, N., Bardhan, K., Chatterjee, P., Sari, D., Liu, B., Bell, L.N., Karoly, E.D., Freeman, G.J., Petkova, V., Seth, P., et al. (2015). PD-1 alters T-cell metabolic reprogramming by inhibiting glycolysis and promoting lipolysis and fatty acid oxidation. *Nat. Commun.* 6, 6692. <https://doi.org/10.1038/ncomms7692>.

100. Sena, L.A., Li, S., Jairaman, A., Prakriya, M., Ezponda, T., Hildeman, D.A., Wang, C.R., Schumacker, P.T., Licht, J.D., Perlman, H., et al. (2013). Mitochondria are required for antigen-specific T cell activation through reactive oxygen species signaling. *Immunity* 38, 225–236. <https://doi.org/10.1016/j.immuni.2012.10.020>.
101. Mehta, M.M., Weinberg, S.E., and Chandel, N.S. (2017). Mitochondrial control of immunity: beyond ATP. *Nat. Rev. Immunol.* 17, 608–620. <https://doi.org/10.1038/nri.2017.66>.
102. van der Windt, G.J.W., Everts, B., Chang, C.H., Curtis, J.D., Freitas, T.C., Amiel, E., Pearce, E.J., and Pearce, E.L. (2012). Mitochondrial respiratory capacity is a critical regulator of CD8+ T cell memory development. *Immunity* 36, 68–78. <https://doi.org/10.1016/j.immuni.2011.12.007>.
103. Bengsch, B., Johnson, A.L., Kurachi, M., Odorizzi, P.M., Pauken, K.E., Attanasio, J., Stelekati, E., McLane, L.M., Paley, M.A., Delgoffe, G.M., et al. (2016). Bioenergetic insufficiencies due to metabolic alterations regulated by the inhibitory receptor PD-1 are an early driver of CD8(+) T cell exhaustion. *Immunity* 45, 358–373. <https://doi.org/10.1016/j.immuni.2016.07.008>.
104. Renner, K., Singer, K., Koehl, G.E., Geissler, E.K., Peter, K., Siska, P.J., and Kreutz, M. (2017). Metabolic hallmarks of tumor and immune cells in the tumor microenvironment. *Front. Immunol.* 8, 248. <https://doi.org/10.3389/fimmu.2017.00248>.
105. Yu, Y.R., Imrichova, H., Wang, H., Chao, T., Xiao, Z., Gao, M., Rincon-Restrepo, M., Franco, F., Genolet, R., Cheng, W.C., et al. (2020). Disturbed mitochondrial dynamics in CD8+ TILs reinforce T cell exhaustion. *Nat. Immunol.* 21, 1540–1551. <https://doi.org/10.1038/s41590-020-0793-3>.
106. Vardhana, S.A., Hwee, M.A., Berisa, M., Wells, D.K., Yost, K.E., King, B., Smith, M., Herrera, P.S., Chang, H.Y., Satpathy, A.T., et al. (2020). Impaired mitochondrial oxidative phosphorylation limits the self-renewal of T cells exposed to persistent antigen. *Nat. Immunol.* 21, 1022–1033. <https://doi.org/10.1038/s41590-020-0725-2>.
107. Zhang, L., and Romero, P. (2018). Metabolic control of CD8+ T cell fate decisions and antitumor immunity. *Trends Mol. Med.* 24, 30–48. <https://doi.org/10.1016/j.molmed.2017.11.005>.
108. Scharping, N.E., Menk, A.V., Moreci, R.S., Whetstone, R.D., Dadey, R.E., Watkins, S.C., Ferris, R.L., and Delgoffe, G.M. (2016). The tumor microenvironment represses T cell mitochondrial biogenesis to drive intratumoral T cell metabolic insufficiency and dysfunction. *Immunity* 45, 374–388. <https://doi.org/10.1016/j.immuni.2016.07.009>.
109. Pearce, E.L., Walsh, M.C., Cejas, P.J., Harms, G.M., Shen, H., Wang, L.S., Jones, R.G., and Choi, Y. (2009). Enhancing CD8 T-cell memory by modulating fatty acid metabolism. *Nature* 460, 103–107. <https://doi.org/10.1038/nature08097>.
110. Chang, C.H., Curtis, J.D., Maggi, L.B., Faubert, B., Villarino, A.V., O'Sullivan, D., Huang, S.C.-C., van der Windt, G.J.W., Blagih, J., Qiu, J., et al. (2013). Posttranscriptional control of T cell effector function by aerobic glycolysis. *Cell* 153, 1239–1251. <https://doi.org/10.1016/j.cell.2013.05.016>.
111. Xu, K., Yin, N., Peng, M., Stamatopoulos, E.G., Shyu, A., Li, P., Zhang, X., Do, M.H., Wang, Z., Capistrano, K.J., et al. (2021). Glycolysis fuels phosphoinositide 3-kinase signaling to bolster T cell immunity. *Science* 371, 405–410. <https://doi.org/10.1126/science.abb2683>.
112. Howie, D., Cobbold, S.P., Adams, E., Bokum, A. ten, Necula, A.S., Zhang, W., Huang, H., Roberts, D.J., Thomas, B., Hester, S.S., et al. (2017). Foxp3 drives oxidative phosphorylation and protection from lipotoxicity. *JCI Insight* 2, e89160. <https://doi.org/10.1172/jci.insight.89160>.
113. Samartsev, V.N., Kozhina, O., Marchik, E.I., and Shamagulova, L. (2011). Involvement of phosphate carrier as a part of complex with ADP/ATP and aspartate/glutamate antiporters in palmitic acid-induced uncoupling in liver mitochondria. *Biochem. Mosc. Suppl. Ser. A Membr. Cell Biol.* 5, 162–169. <https://doi.org/10.1134/S1990747811020061>.
114. Rizzuto, R., Pinton, P., Carrington, W., Fay, F.S., Fogarty, K.E., Lifshitz, L.M., Tuft, R.A., and Pozzan, T. (1998). Close contacts with the endoplasmic reticulum as determinants of mitochondrial Ca2+ responses. *Science* 280, 1763–1766. <https://doi.org/10.1126/science.280.5370.1763>.
115. Trebak, M., and Kinet, J.P. (2019). Calcium signalling in T cells. *Nat. Rev. Immunol.* 19, 154–169. <https://doi.org/10.1038/s41577-018-0110-7>.
116. Long, A.H., Haso, W.M., Shern, J.F., Wanhaninen, K.M., Murgai, M., Ingaramo, M., Smith, J.P., Walker, A.J., Kohler, M.E., Venkateshwara, V.R., et al. (2015). 4-1BB costimulation ameliorates T cell exhaustion induced by tonic signaling of chimeric antigen receptors. *Nat. Med.* 21, 581–590. <https://doi.org/10.1038/nm.3838>.
117. Dumauthioz, N., Tschumi, B., Wenés, M., Martí, B., Wang, H., Franco, F., Li, W., Lopez-Mejia, I.C., Fajas, L., Ho, P.C., et al. (2021). Enforced PGC-1 $\alpha$  expression promotes CD8 T cell fitness, memory formation and anti-tumor immunity. *Cell. Mol. Immunol.* 18, 1761–1771. <https://doi.org/10.1038/s41423-020-0365-3>.
118. Pucino, V., Certo, M., Bulusu, V., Cucchi, D., Goldmann, K., Pontarini, E., Haas, R., Smith, J., Headland, S.E., Blighe, K., et al. (2019). Lactate buildup at the site of chronic inflammation promotes disease by inducing CD4+ T cell metabolic rewiring. *Cell Metab.* 30, 1055–1074.e8. <https://doi.org/10.1016/j.cmet.2019.10.004>.
119. Puleston, D.J., Baixauli, F., Sanin, D.E., Edwards-Hicks, J., Villa, M., Kabat, A.M., Kamiński, M.M., Stanckzak, M., Weiss, H.J., Grzes, K.M., et al. (2021). Polyamine metabolism is a central determinant of helper T cell lineage fidelity. *Cell* 184, 4186–4202.e20. <https://doi.org/10.1016/j.cell.2021.06.007>.
120. Fu, G., Guy, C.S., Chapman, N.M., Palacios, G., Wei, J., Zhou, P., Long, L., Wang, Y.D., Qian, C., Dhungana, Y., et al. (2021). Metabolic control of TFH cells and humoral immunity by phosphatidylethanolamine. *Nature* 595, 724–729. <https://doi.org/10.1038/s41586-021-03692-z>.
121. Coutzac, C., Jouniaux, J.M., Paci, A., Schmidt, J., Mallardo, D., Seck, A., Asvatourian, V., Cassard, L., Saulnier, P., Lacroix, L., et al. (2020). Systemic short chain fatty acids limit antitumor effect of CTLA-4 blockade in hosts with cancer. *Nat. Commun.* 11, 2168. <https://doi.org/10.1038/s41467-020-16079-x>.
122. Hopkins, B.D., Goncalves, M.D., and Cantley, L.C. (2020). Insulin–PI3K signalling: an evolutionarily insulated metabolic driver of cancer. *Nat. Rev. Endocrinol.* 16, 276–283. <https://doi.org/10.1038/s41574-020-0329-9>.
123. Dudek, M., Pfister, D., Donakonda, S., Filpe, P., Schneider, A., Laschinger, M., Hartmann, D., Hüser, N., Meiser, P., Bayerl, F., et al. (2021). Auto-aggressive CXCR6+ CD8 T cells cause liver immune pathology in NASH. *Nature* 592, 444–449. <https://doi.org/10.1038/s41586-021-03233-8>.
124. Schneider, C.A., Rasband, W.S., and Eliceiri, K.W. (2012). NIH Image to ImageJ: 25 years of image analysis. *Nat. Methods* 9, 671–675. <https://doi.org/10.1038/nmeth.2089>.
125. Peng, T., Thorn, K., Schroeder, T., Wang, L., Theis, F.J., Marr, C., and Navab, N. (2017). A BaSiC tool for background and shading correction of optical microscopy images. *Nat. Commun.* 8, 14836. <https://doi.org/10.1038/ncomms14836>.
126. Ouyang, Y., Liu, Y., Wang, Z.M., Liu, Z., and Wu, M. (2021). FLIM as a promising tool for cancer diagnosis and treatment monitoring. *Nanomicro Lett.* 13, 133. <https://doi.org/10.1007/s40820-021-00653-z>.
127. Datta, R., Heaster, T.M., Sharick, J.T., Gillette, A.A., and Skala, M.C. (2020). Fluorescence lifetime imaging microscopy: fundamentals and advances in instrumentation, analysis, and applications. *J. Biomed. Opt.* 25, 1. <https://doi.org/10.1117/1.JBO.25.7.071203>.
128. Love, M.I., Huber, W., and Anders, S. (2014). Moderated estimation of fold change and dispersion for RNA-seq data with DESeq2. *Genome Biol.* 15, 550. <https://doi.org/10.1186/s13059-014-0550-8>.
129. Subramanian, A., Tamayo, P., Mootha, V.K., Mukherjee, S., Ebert, B.L., Gillette, M.A., Paulovich, A., Pomeroy, S.L., Golub, T.R., Lander, E.S., et al. (2005). Gene set enrichment analysis: a knowledge-based approach for interpreting genome-wide expression profiles. *Proc. Natl. Acad. Sci. USA* 102, 15545–15550. <https://doi.org/10.1073/pnas.0506580102>.
130. Liberzon, A., Birger, C., Thorvaldsdóttir, H., Ghandi, M., Mesirov, J.P., and Tamayo, P. (2015). The molecular signatures database (MSigDB)

- hallmark gene set collection. *Cell Syst.* 1, 417–425. <https://doi.org/10.1016/j.cels.2015.12.004>.
131. Langfelder, P., and Horvath, S. (2008). WGCNA: an R package for weighted correlation network analysis. *BMC Bioinformatics* 9, 559. <https://doi.org/10.1186/1471-2105-9-559>.
132. Subramanian, A., Tamayo, P., Mootha, V.K., Mukherjee, S., Ebert, B.L., Gillette, M.A., Paulovich, A., Pomeroy, S.L., Golub, T.R., Lander, E.S., et al. (2005). Gene set enrichment analysis: a knowledge-based approach for interpreting genome-wide expression profiles. *Proc. Natl. Acad. Sci. USA* 102, 15545–15550. <https://doi.org/10.1073/pnas.0506580102>.
133. Gudipati, V., Rydzek, J., Doel-Perez, I., Gonçalves, V.D.R., Scharf, L., Königsberger, S., Lobner, E., Kunert, R., Einsele, H., Stockinger, H., et al. (2020). Inefficient CAR-proximal signaling blunts antigen sensitivity. *Nat. Immunol.* 21, 848–856. <https://doi.org/10.1038/s41590-020-0719-0>.
134. Gao, Y., and Kilfoil, M.L. (2009). Accurate detection and complete tracking of large populations of features in three dimensions. *Opt. Express* 17, 4685–4704. <https://doi.org/10.1364/OE.17.004685>.
135. Salles, A., Billaudeau, C., Sergé, A., Bernard, A.M., Phélypot, M.C., Bertiaux, N., Fallet, M., Grenot, P., Marguet, D., He, H.T., et al. (2013). Barcoding T cell calcium response diversity with methods for automated and accurate analysis of cell signals (MAAACS). *PLoS Comput. Biol.* 9, e1003245. <https://doi.org/10.1371/journal.pcbi.1003245>.
136. Schrimpe-Rutledge, A.C., Codreanu, S.G., Sherrod, S.D., and McLean, J.A. (2016). Untargeted metabolomics strategies-challenges and emerging directions. *J. Am. Soc. Mass Spectrom.* 27, 1897–1905. <https://doi.org/10.1007/s13361-016-1469-y>.
137. Sud, M., Fahy, E., Cotter, D., Brown, A., Dennis, E.A., Glass, C.K., Merrill, A.H., Murphy, R.C., Raetz, C.R.H., Russell, D.W., et al. (2007). LMSD: LIPID MAPS structure database. *Nucleic Acids Res.* 35, D527–D532. <https://doi.org/10.1093/nar/gkl838>.
138. Chong, J., Soufan, O., Li, C., Caraus, I., Li, S., Bourque, G., Wishart, D.S., and Xia, J. (2018). MetaboAnalyst 4.0: towards more transparent and integrative metabolomics analysis. *Nucleic Acids Res.* 46, W486–W494. <https://doi.org/10.1093/nar/gky310>.
139. Wieckowski, M.R., Giorgi, C., Lebiedzinska, M., Duszynski, J., and Pinton, P. (2009). Isolation of mitochondria-associated membranes and mitochondria from animal tissues and cells. *Nat. Protoc.* 4, 1582–1590.

## STAR★METHODS

### KEY RESOURCES TABLE

REAGENT or RESOURCE	SOURCE	IDENTIFIER
<b>Antibodies</b>		
anti-human CD127 - APC R700	BD Biosciences	CAT#565185, RRID: AB_2739099
anti-human CD25 - BV421	BD Biosciences	CAT#562442, RRID: AB_11154578
anti-human CD27 - BV786	BD Biosciences	CAT#563327, RRID: AB_2744353
anti-human CD3 - BB700	BD Biosciences	CAT#566575, RRID: AB_2860004
anti-human CD45 - BV605	BD Biosciences	CAT#564047, RRID: AB_2744403
anti-human CD45RA - PE	BD Biosciences	CAT#561883, RRID: AB_10895572
anti-human CD45RO - PE Cy7	BD Biosciences	CAT#560608, RRID: AB_1727499
anti-human CD62L - BV650	BD Biosciences	CAT#743210, RRID: AB_2741346
anti-human CD69 - APC Cy7	BD Biosciences	CAT#560912, RRID: AB_10563414
anti-human CD8 - APC	BD Biosciences	CAT#561952, RRID: AB_10897996
anti-human CD8 - BV786	BD Biosciences	CAT#563823, RRID: AB_2687487
anti-human PD1 - BV650	BD Biosciences	CAT#564104, RRID: AB_2738595
anti-human PD1 - BV786	BD Biosciences	CAT#563789, RRID: AB_2738425
anti-mouse CD127 - PE	BD Biosciences	CAT#552543, RRID: AB_394417
anti-mouse CD127 - PECF594	BD Biosciences	CAT#562419, RRID: AB_11153131
anti-mouse CD137 - BV421	BD Biosciences	CAT#740033, RRID: AB_2739805
anti-mouse CD25 - BV650	BD Biosciences	CAT#564021, RRID: AB_2738547
anti-mouse CD3e - APC	BD Biosciences	CAT#553066, RRID: AB_398529
anti-mouse CD44 - BV786	BD Biosciences	CAT#563736, RRID: AB_2738395
anti-mouse CD44 - APC Cy7	BD Biosciences	CAT#560568, RRID: AB_1727481
anti-mouse CD45 - redFluor710	Tonbo	CAT#80-0451-U100
anti-mouse CD45 - Pacific Blue	Biolegend	CAT#103126, RRID: AB_493535
anti-mouse CD45 - APC Cy7	BD Biosciences	CAT#561037, RRID: AB_10563075
anti-mouse CD62L - BV605	BD Biosciences	CAT#563252, RRID: AB_2738098
anti-mouse CD62L - BV786	BD Biosciences	CAT#564109, RRID: AB_2738598
anti-mouse CD62L - APC R700	BD Biosciences	CAT#565159, RRID: AB_2737397
anti-mouse CD69 - PECF594	BD Biosciences	CAT#562455, RRID: AB_11154217
anti-mouse CD8a - V450	BD Biosciences	CAT#560469, RRID: AB_1645281
anti-mouse CD8a - PE Cy7	BD Biosciences	CAT#561097, RRID: AB_2034013
anti-mouse CXCR3 - BV421	BD Biosciences	CAT#562937, RRID: AB_2687551
anti-mouse EOMES - eFluor660	Invitrogen	CAT#50-4875-82, RRID: AB_2574227
anti-mouse EOMES - AFUor488	eBioscience	CAT#53-4875-82, RRID: AB_10854265
anti-mouse Granzyme B - FITC	eBioscience	CAT#11-8898-82, RRID: AB_10733414
anti-mouse IFNg - PECF594	BD Biosciences	CAT#562303, RRID: AB_11153140
anti-mouse IFNg - BV786	BD Biosciences	CAT#563773, RRID: AB_2738419
anti-mouse IL2 - BV605	BD Biosciences	CAT#563911, RRID: AB_2738482
anti-mouse IP3R1	EMD Millipore	CAT#AB5882, RRID: AB_92113
anti-mouse KLRG1 - BV650	BD Biosciences	CAT#740553, RRID: AB_2740254
anti-mouse LAG3 - BV650	BD Biosciences	CAT#740560, RRID: AB_2740261
anti-mouse PD1 - BV421	BD Biosciences	CAT#748268, RRID: AB_2872696
anti-mouse PD1 - FITC	Biolegend	CAT#135214, RRID: AB_10680238
anti-mouse Perforin - APC	Biolegend	CAT#154403, RRID: AB_2721464
anti-mouse Tbet - PE	BD Biosciences	CAT#561268, RRID: AB_10564071
anti-mouse TCF1 - PE	BD Biosciences	CAT#564217, RRID: AB_2687845

(Continued on next page)

**Continued**

REAGENT or RESOURCE	SOURCE	IDENTIFIER
anti-mouse TCF1 - APC	BD Biosciences	CAT#566693, RRID: AB_2869823
anti-mouse TCR Vb5.2, 5.2 - PE	Biolegend	CAT#139504, RRID: AB_10613279
anti-mouse TCR Vb5.2, 5.2 - FITC	Biolegend	CAT#139514, RRID: AB_2750133
anti-mouse TIM3 - BV786	BD Biosciences	CAT#747621, RRID: AB_2744187
anti-mouse TNF - BV650	BD Biosciences	CAT#563943, RRID: AB_2738498
anti-mouse/human TOX - APC	Miltenyi Biotec	CAT#130-118-335, RRID: AB_2751485
CFSE	BD Biosciences	CAT#565082, RRID: AB_2869649
CD3 Monoclonal Antibody (OKT3)	Invitrogen	CAT#16-0037-81, RRID: AB_468854
Cleaved Caspase-3 (Asp175)	Cell signaling	CAT#9661, RRID: AB_2069869
Far-Red Fluorescent Live-Cell Impermeant	BioStatus Limited	DR71000
DNA Dye DRAQ7		
Fixable Viability Dye 640/662	Biotum	32007A
Fixable viability Stain 510	BD Biosciences	CAT#564406, RRID: AB_2869572
GRP78	Invitrogen	CAT#PA1014A, RRID: AB_559362
Histone H3	Abcam	CAT#ab1791, RRID: AB_302613
OXPHOS	Abcam	CAT#ab110413, RRID: AB_2629281
Phospho-s6 Ser240/244	Cell signaling	CAT#5364, RRID: AB_10694233
Purified anti-human Cd28	BD Biosciences	CAT#556620, RRID: AB_396492
Purified anti-human Cd3	BD Biosciences	CAT#551916, RRID: AB_394293
Purified anti-mouse Cd28	BD Biosciences	CAT#553294, RRID: AB_394763
Purified anti-mouse Cd3	BD Biosciences	CAT#553057, RRID: AB_394590
Alexa488-affini Donkey Anti-rabbit IgG	Invitrogen	CAT#A-21206, RRID: AB_2535792
VDAC (D73D12)	Cell signaling	CAT#4661, RRID: AB_10557420
Vinculin	Sigma	CAT#V9131, RRID: AB_477629
APC Goat anti-Mouse IgG	Invitrogen	CAT#A-865, RRID: AB_141364
<b>Chemical, peptides, and recombinant proteins</b>		
2-mercaptoethanol	Invitrogen	31350010-50mM
4 Diamidino 2 Phenylindole	Sigma	32670-25MG-F
4-phenylbutyric Acid	Sigma	P21005
ACK Lysing buffer	Invitrogen	A10492
Albumin Bovine Fraction	Sigma	A8806
Approved Fbs South American	EuroClone SpA	ECS0165L
Arachidonic Acid- BSA conjugated	Aurogene	OOCDD00263
Calcein AM	Life technologies	C3100MP
Colegenase from C. histolyticum	Sigma	C2674-1G
CTS OpTmizer T Cell medium	Invitrogen	A1048501
D-( )-glucose Solution	Sigma	G8769
Deoxyribonuclease I	Sigma	D5025-375KU
Etomoxir	Sigma	E1905-5MG
Ficoll Paque Plus	Sigma	GE17-1440-03
GolgiPlug	BD Biosciences	555029
Hcs Lipidtox Red Neutral Lipid Stain	Life technologies	H34476
Hoechst No. 33342	Sigma	B2261
human AB serum	AnProtec	ACSM0071
Ionomycin	Sigma	I0634
Linoleic Acid - BSA conjugated	Sigma	L9530
MitoTracker Green FM	Invitrogen	M7514
MitoTracker Orange CMTMRos	Invitrogen	M7510
Nocodazole	Sigma	M1404

(Continued on next page)

**Continued**

REAGENT or RESOURCE	SOURCE	IDENTIFIER
Oleic Acid - BSA conjugated	Sigma	O3008
OVA peptide (SIINFEKL)	SB-Peptide	N/A
Paraformaldehyde	Invitrogen	043368.9L
Penicillin/Streptomycin 100X	EuroClone SpA	ECB3001D
PMA	Sigma	P1585
Recombinant human Interleukin 15	Miltenyi	130-095-762
Recombinant human Interleukin 2	Novartis	CLB-P-476-800-13980 IT
Recombinant human Interleukin 7	Miltenyi	130-095-361
Rpmi 1640 With Stable L-glutamine	EuroClone SpA	ECM2001L
Seahorse Xf Ph 7.4 Rpmi	Agilent	103681-100
Sodium Pyruvate Solution 100 Nm	EuroClone SpA	LOBE13115E
Thapsigargin	Sigma	T9033
Triton X100	Vwr International	1.08603.1000
U-13C18 Linoleic acid	Cambridge Isotopes	CLM-6855
<b>Critical commercial assays</b>		
Acetyl-Coenzyme A Assay Kit	Sigma	MAK039
Atp 1 Determination Kit	Invitrogen	A22066
BCA Protein Assay kit	ThermoScientific	23227
CD8+ T cell isolation Kit Human	Miltenyi	130-096-495
CD8+ T cell isolation Kit Mouse	Miltenyi	130-104-075
Clarity Western ECL substrate	Biorad	170-5061
Foxp3 Fix/perm Buffer Set	BD Biosciences	560409
Lactate Assay Kit	Sigma	MAK064
LS columns	Miltenyi	130-042-401
RetroNectin	Takara-Bio	T110A
Rneasy Minielute Cleanup Kit	Qiagen	74204
Seahorse Xf Cell Mito Stress Test Kit	Agilent	103015-100
Seahorse Xf Glycolytic Rate Test Kit	Agilent	103344-100
Seahorse Xfe96 Fluxpak Mini	Agilent	102601-100
Ultracomp Ebeads Affymetrix	Invitrogen	01-2222-42
<b>Deposited data</b>		
RNAseq data	ArrayExpress database	ArrayExpress: E-MTAB-12645
<b>Experimental models: Cell lines</b>		
Cell line: B16-OVA	Dr. Paolo Dellabona	N/A
Cell line: 293T	ATCC	CAT#CRL-3216, RRID: CVCL_0063
Cell line: 4T1	ATCC	CAT#CRL-2539, RRID: CVCL_0125
Cell line: B16-F10	ICLC	CAT#ATL99010, RRID: CVCL_0159
Cell line: CT26WT	ATCC	CAT#CRL-2638, RRID: CVCL_7256
Cell line: Karpas 299	ECACC	CAT#06072604, RRID: CVCL_1324
Cell line: MC38	Dr. Marina Mapelli	N/A
Cell line: Raji	DSMZ	CAT#ACC-319, RRID: CVCL_0511
Cell line: SH-SY5Y	DSMZ	CAT#ACC-209, RRID: CVCL_0019
Healthy adult buffycoats (male/female)	University Hospital Würzburg, Germany	250/20-am
<b>Experimental models: Organisms/strains</b>		
C57BL/6 (female)	Charles Rivers	Strain code: 027
C57BL/6-Tg(TcrαTcrβ)1100Mjb/Crl	Charles Rivers	Strain code: 642
<b>Software and algorithms</b>		
FLowJo v10.2	Tree Star	RRID: SCR_008520

(Continued on next page)

**Continued**

REAGENT or RESOURCE	SOURCE	IDENTIFIER
Gene Set Enrichment Analysis	UC San Diego - Broad Institute	RRID: SCR_003199
GraphPad Prism 7.0	GraphPad software	RRID: SCR_002798
Huygens software	Scientific Volume Imaging	RRID: SCR_014237
ImageJ	NIH	RRID: SCR_003070
Ingenuity Pathway Analysis	Qiagen	RRID: SCR_008653
Lipid Maps database	Wellcome Trust	RRID: SCR_003062
MATLAB	The MathWorks	RRID: SCR_001622
Metaboanalyst 4.0	NIH - Canada Research Chair	RRID: SCR_015539
SeaHorse analytics	Agilent	RRID: SCR_019545
SymPhoTime 64	PicoQuant	RRID: SCR_016263

## RESOURCE AVAILABILITY

### Lead contact

Further information and requests for resources and reagents should be directed to the lead contact Teresa Manzo ([Teresa.manzo@ieo.it](mailto:Teresa.manzo@ieo.it)).

### Materials availability

All the materials generated and used in this study will be available upon request.

### Data and code availability

- All data reported in this paper will be shared by the lead contact upon request. RNA-seq data are available into the ArrayExpress database under accession codes E-MTAB-12645.
- Uncropped scans of all Western blots and all raw data used to generate graphs are included in [Data S1](#).
- This paper does not report original code.
- Any additional information required to reanalyze the data reported in this paper is available from the lead contact upon request.

## EXPERIMENTAL MODEL AND SUBJECT DETAILS

The use of human samples was approved by the European Institute of Oncology (IEO) Ethical Committee (registered as IEO 1781). All donors provided written informed consent in accordance with the Declaration of Helsinki. Mice were housed and bred in a specific-pathogen-free animal facility and treated in accordance with the European Union Guideline on Animal Experiments under the protocol number #566/21. For mouse experiments, we used age-matched (8–10 weeks) C57BL/6J or OT1 female mice in each experiment. The number of animals (biological replicates) was indicated in the respective figure legends.

## METHOD DETAILS

### CD8<sup>+</sup> T cell isolation and activation

Spleen and lymph nodes (inguinal and axillary) were harvested from mice under sterile conditions, mechanically dissociated into single cell suspension and red blood cells were lysed. Cells were then sorted by negative selection following the manufacturer's instructions. After sorting, cells were resuspended at 1 × 10<sup>6</sup> cells/mL in complete RPMI media (10% FBS, 1% NaPy, 1% Glutamine, 1% Pen/Strep, 0.1% β-mercaptoethanol) supplemented with 100U/mL IL2. For OT1 mice, media was further complemented with 2 μg/mL of SIINFEKL peptide, while for C57J/B6 mice polyclonal activation was achieved using 5 μg/mL plated-bound αCD3 and 0.5 μg/mL soluble αCD28. Cells were further treated with BSA, linoleic acid, oleic acid or arachidonic acid. Unless otherwise specified, the final concentration for each lipid was kept at 100 μM. For high glucose experiments, T cell media was supplemented with 12 mM D-(+)-glucose (twice as physiological conditions). Unless otherwise specified, cells were activated for 48 hours at 37°C, 5% CO<sub>2</sub> and 90–95% humidity for a pH neutral environment.

### Immunophenotype and flow cytometry

Characterization of the activation and differentiation profile of LA-CTL was performed by flow cytometry following standard protocols. Briefly, for staining of surface markers 1 × 10<sup>5</sup> – 2 × 10<sup>6</sup> cells were harvested at the specified post-activation time points, washed with PBS, resuspended in FACS buffer (PBS, 1% FBS, EDTA 2mM) and stained for 20 minutes at 4°C. Intracellular staining for cytokine production was performed following a 4 hours incubation with complete RPMI and 1:1000 dilution of GlogiPlug in the presence or

absence of a secondary stimulation with SIIINFELK peptide (5 µg/mL) or PMA/Ionomycin (20 ng/mL and 1 µg/mL respectively) at 37°C. Cells were fixed and permeabilized following manufacturer's instruction. Intracellular staining was then performed in permeabilization buffer for 2 hour at 4°C. CFSE; MitoTRK Orange and Green; and HCS LipidTOX stainings were performed as per manufacturer's instructions. The expression of GD2.CAR on T cells was detected using a specific anti-idiotype antibody (1A7) while for the CD30 and CD19.CAR detection a biotinylated human CD30 or CD19 protein has been used (Acro Biosystems, Newark, DE – USA). Samples were acquired with a BD FACS Canto II or Celesta.

### tSNE analysis

FCS data was analysed with software FlowJo v10.2. RPhenograph package was used to perform computational analysis of multiparametric flow cytometry data. 3000 events per sample were concatenated by the “cytof\_expsMerge function”, after manual gating isolation of singlet, LD negative CD45<sup>+</sup>CD3<sup>+</sup>CD8<sup>+</sup> T cells. All samples were concatenated by the “cytof\_expsMerge function”. ). The number of nearest neighbours identified in the first iteration of the algorithm, K value, was set to 100. UMAP and tSNE representation were generated and visualized using FlowJo version 10.2. Under-represented clusters (<0.5%) were discarded in subsequent analysis.

### Immunofluorescence and confocal microscopy

Confocal microscopy with fixed cells was performed on a LEICA SP8 FSU confocal (Leica Microsystems GmbH, Wetzlar, Germany) microscope (Imaging Unit, IEO) with a 40X/1.3, 63X/1.4 or 100X/1.47 oil- immersion objectives. Cells were pre-stained with MitoOr. and a fixable viability dye; allowed to attach by gravity on culture slides coated with poly-d-lysine; and then fixed with 4% paraformaldehyde and permeabilized with 0.1% Triton X-100. IP3R IC staining was performed overnight at 4°C in blocking buffer (PBS, Triton 0.1%, 3% BSA and 5% FBS) and afterwards cells were counterstained with DAPI and the indicated secondary antibody for 2 hours at room temperature.

For static killing experiments, B16-OVA cells were plated on a Lab-Tek II chamber slide and left to adhere for 6 hours prior to co-culture with activated CD8<sup>+</sup> T cells. OT1 CTL activated in the presence or absence of LA for 48 hours were then counted and added to the chamber in a Effector: Target (E:T) ratio of 1:1. 12 hours post-co-culture, chambers were washed, stained with a fixable viability dye and  $\alpha$ CD8 for 30 min at 4°C in PBS; fixed and permeabilized as previously described. Cells were then stained with primary antibody  $\alpha$ Caspase 3 overnight at 4°C, labelled with the appropriate secondary antibody, and counterstained with DAPI for 2 hours at room temperature.

For colocalization analysis, a multi-channel Z-stack of 2.5 um of the central part of the cells was acquired for each field of view with a 63x/1.4NA oil immersion objective lens and a voxel size of 60x60x180nm. DAPI, anti-IP3R labelled with an AlexaFluor488 labelled secondary antibody, MitoOr. and DRAQ7 signals were excited with 405 nm, 488 nm, 568 nm, 633 nm laser lines and the emitted fluorescence acquired in the following acquisition windows: 410-512, 495-545, 566-668, 638-775 nm, respectively. The Z-stacks were deconvolved with Huygens software and the central section of each cell was used to calculate the percentage of colocalization. A macro in Fiji/ImageJ<sup>124</sup> has been created. Briefly, region of interests (ROIs) including only one cell were split in the single fluorescent channels, the IP3R and MitoOr. channels were segmented using the Moments and Otsu algorithm, respectively, and the area occupied by the two signals was calculated. The colocalization area was calculated as the interception between the IP3R and the MitoTracker Orange binary images and expressed as percentage respect to the total area occupied by the mitochondria.

### Time-lapse microscopy

For time-lapse killing experiments B16-OVA cells were pre-stained with Hoechst33342 solution at 37°C for 30 minutes before plating on a pre-coated Ibidi chamber slide and left to adhere for 8 hours. OT1 cells were activated in the presence or absence of LA; with or without TG for 12 or 48 hours and stained using 1 $\mu$ M Calcein AM at 37°C for 30 minutes. CTL were then put in co-culture with tumor cells at E:T ratios of 1:1 or 1:4 as specified. DRAQ7 dye was added directly to the chambers to follow cell death in real time using a Leica Thunder Imager microscope equipped with a Okolab incubation system (Okolab S.r.l. Naples, Italy). Acquisitions were made every 15 minutes for a total of 5 hours and 8-9 randomly assigned fields were acquired for each chamber. Time-lapse hyper-stacks were processed with Fiji/ImageJ and a custom macro. Briefly, Hoechst, calcein and DRAQ7 channels were processed for shading correction using the BaSiC tool.<sup>125</sup> Then, tumor cells were segmented thanks to the Hoechst staining and the DRAQ7 signal was measured in the segmented cells. Results tables were analysed with the R software. The number of dead cells at each time-point was corrected for the number of dead cells at the first time-point and the percentage of dead cells calculated respect to the total number of cells.

### Fluorescence lifetime imaging microscopy (FLIM)

OT1 cells were sorted with >95% purity as previously described, activated for 48 hours in the presence or absence of LA and 5x10<sup>5</sup> cells were seeded on a Poly-Lysine coated coverslip and let to adhere for 30 min at 37°C. Fixation was performed using following manufacturer's instructions. NAD(P)H Fluorescence Lifetime Imaging Microscopy<sup>126,127</sup> was performed using an OLYMPUS Fluoview FV3000 system (Shinjuku, Tokyo, Japan) equipped with a pulsed 372 nm laser from PicoQuant (Berlin, Germany). The laser was operated at 40 MHz and photons were detected by a photon counting detector (Photomultiplier Detector Assembly Hybrid Series, PicoQuant, Berlin, Germany). Photons were collected from two randomly chosen fields from each well of each condition (10 minutes each, 60x magnification, 256x256 pixels). Fluorescence decay data were acquired using SymPhoTime 64 software.

The raw data were converted to TIFF format, imported into MATLAB and processed using a custom script. A triexponential curve was fitted to the averaged decay curve of all pixels with a photon count greater than 100. The resulting decay coefficients were 1.645 ns (assigned to protein-bound NAD(P)H), 0.400 ns (assigned to free NAD(P)H), and 6.814 ns (unassigned, but observed also in control NADH + lactate dehydrogenase solutions). NADH and NADPH have the same spectral properties and thus the acronym “NAD(P)H” was used to indicate their combination.<sup>127</sup> Fluorescence lifetimes were consistent with the lifetimes previously reported for bound and free NAD(P)H.<sup>127</sup> The pre-exponential factors of the averaged decay curve of each field (obtained from pixels with a photon count >100) were fitted with a triexponential curve, using the global decay coefficients as fixed parameters. The ratio between the pre-exponential coefficients of protein-bound NAD(P)H and free NAD(P)H was calculated for each field. An increase in the protein bound/free NAD(P)H ratio corresponds to a shift from a glycolytic towards an OXPHOS metabolism.<sup>126</sup> Protein bound/Free NAD(P)H ratios referring to the same condition of each mouse were averaged.

### Metabolic assays

A Seahorse XF-96e extracellular flux analyser (Seahorse Bioscience, Agilent) was used to determine the metabolic profile of cells. OT1 CD8<sup>+</sup> T cells were plated (2x10<sup>5</sup> cells/well) onto cell culture microplates coated with poly-lysine. Mitochondrial perturbation experiments were carried out using the MitoStress Test Kit by the sequential treatment with oligomycin (Oligo, 1 μM), FCCP (1.5 μM), and rotenone (Rotenone A + Antimycin, 0,1 μM). Oxygen consumption rates (OCR, pmol/min), proton efflux rate (PER, pmol/min), and extracellular acidification rates (ECAR, mph/min) were monitored in real time after injection of each compound. A variation on the standard MitoStress Test protocol was used to assess the role of FAO in OCR and SRC levels of CD8<sup>+</sup> T cells. Briefly, etomoxir (200 μM) acute injection was performed ahead of the regular MitoStress Test. OCR, PER and ECAR levels were calculated as previously described in treated and non-treated cells (with complete media as acute injection for control). Glycolytic Rate Assay was performed by the sequential injection of Rotenone A + Antimycin A (0,5 μM) and 2-deoxy-D-glucose (2-DG, 50nM) to discriminate between the glycolysis- and mitochondrial-dependent PER.

### Electron microscopy

Transmission electron microscopy was performed at the ALEMBIC Facility (San Raffaele Hospital). Cells were pelleted and fixed in 2,5% glutaraldehyde 0.1M sodium cacodylate pH 7.4 for 1 hour at RT. After fixation cells were rinsed with 0.1 M Cacodylate and post-fixed in 1% OsO<sub>4</sub>, 1.5% K4Fe(CN)6, 0.1M sodium cacodylate for 1h at 4°C. After washes steps cells were dehydrated using ethanol and embedded in Epon. Ultrathin sectioning (70 nm) was performed on a Leica EM UC7 ultramicrotome and collected on 300 mesh grids. Thin sections were contrasted with uranyl acetate and Sato lead stain. Samples were observed with a TALOS L120C Transmission Electron Microscope (ThermoFisher Scientific) and images were acquired with a CETA 4x4k CMOS camera (ThermoFisher Scientific).

### MAM's and ER-mitochondria contact's analysis

From the EM images, the endoplasmic reticulum and mitochondria masks are manually segmented. These masks are analysed with a MATLAB pipeline to identify the contact sites. We first extract information on the single mitochondria: for each mitochondrion mask, the area is expanded in each direction of 30 nm. These contact sites (ER-MAMs) are identified as the intersections of the ER mask that follow within this new area. The ER-MAMs extension is calculated and normalized to mitochondrion perimeter and expressed as percentage. For broad ER-mitochondria contacts the same analysis is performed within a range from mitochondria of 30 to 100nm.

### RNA-seq and analysis

OT1 cells were sorted with >95% purity as previously described, activated for 48 hours in the presence or absence of LA, counted and resuspended in RLT lysis buffer (Qiagen). RNA was isolated from purified cells using RNeasy Mini kits, and RNA concentrations were determined using Nanodrop. Fastqc software was used on the fastq files to generate the quality control report, and Tophat software was used to align the sequences to the mouse genome mm10. HTSeq was used to count the read number of genes from each sample. Genes with read counts <10 in all the samples were considered to be noise and therefore removed. The obtained read counts are analogous to the expression level of each gene across all the samples. Differential expression analysis was performed using DESeq2.<sup>128</sup> Genes with raw mean reads >10 (i.e., ~9,225 genes) were used for normalization and differential gene expression analysis using DESeq2 package in R. The Wald test defined in the DESeq function of the package was used for differential expression and further downstream analysis. PCA, hierarchical clustering plots (hclust), and XY plots between replicates of the same genotypes were used to examine for nominal amounts of nontechnical variation and other latent factors. PCA and volcano plots were generated using ggplot2 package, and all the heatmaps were generated using pheatmap or heatmap2 package in R environment. Gene overlap analysis was performed against the Molecular Signatures Database<sup>129,130</sup> Investigate Gene Sets web program under GSEA. Differentially expressed genes (DEG) are listed in Table S1.

Weighted gene co-expression network analysis (WGCNA) was employed to construct gene co-expression networks across gene expression data, exploring the association between gene networks and external phenotypic/clinical traits of interest.<sup>131</sup> The algorithm builds co-expression networks as undirected, weighted gene networks where nodes correspond to genes and edges between them are determined by the pairwise correlations between their gene expression profiles. By raising the absolute value of the correlation to a power (soft thresholding), the weighted gene co-expression network construction emphasizes high correlations at the expense of low correlations. A reasonable choice to properly set the value of this power is the one that guarantees an approximate

scale-free network topology that is typical of most of biological networks.<sup>131,132</sup> Scale-free networks are extremely heterogeneous with a topology characterized by a few highly connected nodes (hub nodes) and many less connected nodes (peripheral nodes). Then, WGCNA identifies modules (labeled by colors) of highly interconnected, or co-expressed, genes within the weighted network by grouping together the most similar nodes. The similarity measure between two nodes is expressed in terms of their direct connection strength as well as connection strengths “mediated” by shared neighbors. The relationship among modules and their associations with external traits can be studied by correlating the corresponding module eigengenes (MEs). The ME is defined as the first principal component of a given module and can be considered a representative of the gene expression profiles in that module. For each gene, a measure of module membership (MM) is defined by correlating its gene expression profile with the module eigengene of a given module and can be computed for all input genes (irrespective of their original module membership). If MM of a given gene with respect to a given module is close to 0, that gene is not part of that module. On the other hand, if MM is close to 1 or -1, the gene is highly connected to the genes of that module. The sign of MM encodes whether the gene has a positive or a negative relationship with the module eigengene. Finally, to incorporate external information into the co-expression network, WGCNA makes use of gene significance (GS) measures computed as the correlations between gene expressions and external sample traits. Abstractly speaking, the higher the absolute value of GS of a given gene, the more biologically significant is that gene. The gene significance of 0 indicates that the gene is not significant with regard to the biological question of interest. The gene significance can take on positive or negative values. The identified modules (ME) are listed in [Table S2](#).

### Calcium influx

Intracellular changes in Ca<sup>2+</sup> levels were measured using the ratio metric calcium-sensitive dye Fura-2-AM.<sup>133</sup> A total of 9x10<sup>5</sup> cells were incubated in 0.5 mL imaging buffer (HBSS, supplemented with 2mM CaCl<sub>2</sub>, 2mM MgCl<sub>2</sub>, 2% FCS) supplemented with 5 μM Fura-2-AM for 15 min at 37°C, washed twice with 10 ml of imaging buffer and resuspended in 135 μl imaging buffer. Cells were kept at RT for a maximum of 30 minutes prior to starting the experiment. Right before imaging, SLBs buffer was exchanged to imaging buffer prewarmed to 37°C. T-cells were pipetted into the imaging buffer and allowed to sink for 30 seconds after which 510/80 nm emission was recorded with alternating 340 nm and 387 nm excitation every 15 seconds for 20 minutes.

An in-house custom-built MATLAB software was used to track cells in each frame using a particle tracking algorithm published by Gao and Kilfoil.<sup>134</sup> Tracking parameters were chosen so only single cells in contact with the SLB were included. We used the MATLAB software to create ratio images for each frame. ‘Methods for automated and accurate analysis of cell signals’ or MAACS was used for population analysis as described in Salles et al.<sup>135</sup> For each trajectory within a population the ratio was normalized frame-wise to that of the population median of T cells in contact with antigen-free SLBs. Cells that were above the threshold for at least 80% of their trajectory were counted as activated and plotted in a dose-response curve. The calcium histograms were compiled from the measured population values of the median Fura-2-AM ratio corresponding to the first10 frames after the peak Fura-2-AM ratio value within the trajectory. The latter was normalized frame-wise to the population median of the negative control, i.e. cells confronted with antigen-free SLBs.

### Metabolomics and lipidomic assays

Liquid chromatography–MS lipidomic analyses were performed on sorted OT1 cells using reverse-phase liquid chromatography (RPLC) coupled with positive- and negative- mode electrospray-ionization high-resolution MS. Lipids from the samples were extracted using the Folch extraction method. Briefly, cell pellets were resuspended in 100 μl ammonium formate buffer, 50 mM, pH 6.8, followed by the addition of 400 μl ice-cold methanol. Each sample was vortexed and sonicated for 10 pulses at 30% power using a sonication probe while cooling on ice. 800 μl chloroform and 100 μl water were added to each sample to a final ratio of 4:2:1 chloroform: methanol: water. Samples were vortexed, incubated on ice for 10 min, and spun down at 1,000 rpm for 10 min. The bottom layer (organic layer containing the lipids) was transferred to a clean Eppendorf tube, and the extraction with chloroform of the aqueous layer was repeated once. The organic layers (lipid layers) were coupled and dried down under vacuum. Before MS analysis, dried lipids were reconstituted in chloroform: methanol (50:50, vol/ vol) containing an internal heavy labelled lipid standard (Splash Lipidmix Mass Spec Standard; Avanti Polar Lipids) and centrifuged for 5 min at 15,000 rpm. Samples were volume adjusted to ensure that cell count per volume (μl) was normalized. Global untargeted lipidomic analyses were performed using full MS and data-dependent acquisition analyses on a Q-Exactive HF hybrid quadrupole–Orbitrap mass spectrometer (Thermo Fisher Scientific) equipped with a Vanquish UHPLC binary system and auto-sampler (Thermo Fisher Scientific). Extracts (5-μl injection volume for RPLC-POS and 6 μl for RPLC-NEG) were separated by RPLC on a Hypersil Gold 1.9-μm, 2.1 × 100-mm column (Thermo Fisher Scientific) held at 40°C. Reverse-phase separation was performed at 250 μl/min using solvent A (0.1% formic acid in water) and solvent B (0.1% formic acid in isopropanol: acetonitrile: water [60:36:4]) with the following gradient: 30% B for 0.5 min, 30–70% B over 1.5 min, 70–99% B over 13 min, 99–10% B over 1min, 10% Bheld4min, 10–30% Bover1min, and 30% Bheld over 5 min (gradient length 30 min). List of measured metabolites are listed in [Table S3](#).

Ultra-performance liquid chromatography/tandem MS raw data were imported, processed, normalized, and reviewed using Progenesis QI v.2.1 (Non-linear Dynamics). All sample runs were aligned against a quality control pool reference run, and peak picking was performed on individual aligned runs to create an aggregate dataset. Features (retention time and m/z pairs) were combined using both adduct and isotope deconvolution. Data were normalized to the spike-in lipid standards as an abundance ratio. Statistically significant changes were identified using multivariate statistical analysis, including PCA, and P values were generated using ANOVA or pairwise comparison. Tentative annotations<sup>136</sup> were made within Progenesis using accurate mass measurements

(<5 ppm error), isotope distribution similarity, and assessment of fragmentation spectrum matching (when applicable) from the Lipid Maps database.<sup>137</sup> Four biological replicates and two technical replicates from each sample type were used to calculate the fold change and P value, and features were considered differentially expressed only if they met both criteria of fold change  $\geq |2|$  and significance ( $P \leq 0.05$ ). Heatmap visualization of individual lipid features was performed using Metaboanalyst 4.0 software<sup>138</sup> using Pearson average clustering algorithm. To assess instrument performance and reproducibility throughout our experimental run sequence, the retention times and peak areas of SPLASH Lipidomix standards were monitored.

### Total cell lysate preparation and cell fractionation

To prepare cell lysates for protein extraction, cells were activated for 48 hours in the presence or absence of LA. For the total cell protein extract, cell pellets were washed with cold PBS and lysed using RIPA buffer containing protease and phosphatase inhibitors. The subcellular fractionation was performed as previously described by Wieckowski et al.<sup>139</sup> Briefly, 100 M of OT-I T cells were homogenized in hypotonic buffer containing mannitol and sucrose and centrifuge at 600g for 5 min at 4°C to separate nuclei. The supernatant was collected and centrifuged at 7000g at 4°C to collect the MAMs/mitochondrial fraction. The supernatant, containing ER microsomes and lysosomes fraction, was firstly centrifuged at 20000g for 30 min, to discard lysosomes and plasma membrane debris and, subsequently at 100000g for 1 h to obtain pure ER fraction. Pure mitochondria and MAMs were obtained via density-gradient separation with percoll. Pellet was resuspended in cold Mitochondria Resuspension Buffer (MRB), composed as described by Wieckowski et al., 2009 and centrifuge at 95000g for 30 min at 4°C. Different fractions are collected and washed at 6300g for 10 min at 4°C in MRB, then MAMs fraction was concentrated by a further centrifugation at 100000g for 1h at 4°C.

### Immunoblots

Protein concentrations were determined by BCA protein assay kit. Total cell lysates, cytoplasmic, mitochondria–ER junction-enriched mitochondrial fractions or pure mitochondrial fractions were separated using 10% acrylamide gel, and transferred to nitrocellulose membranes. Membranes were probed with antibodies against GR78, VDAC, IP3R or OXPHOS kit. Blots were stained with appropriate secondary antibodies and revealed using peroxide solution.

### Lactate assay

Cell media was collected following 48 hours of T cell activation in the presence or absence of LA centrifuged at 2000 rpm for 10 minutes to remove any cell debris and lactate concentration in the TCM was detected using a colorimetric assay according to manufacturer's instructions.

### Acetyl Co-A assay

CD8<sup>+</sup> T cells were collected and washed in PBS to perform analysis of total and cytoplasmic AcCoA. For extraction of cytoplasmic AcCoA from 1x10<sup>6</sup> T cells sample were homogenized in 1% Triton X-100, 20 mM Tris-HCl, pH=7.4, 150 mM NaCl on ice for 10 min and centrifugated at 20000 g for 10 min at 4°C to pellet nuclei and mitochondria. Supernatant obtained after centrifugation was used to measure the nucleocytosolic fraction. For total cellular AcCoA quantification, cells were wash in PBS and the pellet was extracted with two freezing-thawing cycles on liquid nitrogen 80% methanol or 5% sulfo-salicylic acid with 50µM DTT. Samples were deproteinize with a 10 kDa MWCO spin filter prior to the assay. AcCoA was quantified with Acetyl-Coenzyme A Assay Kit following manufacturer instructions.

### Adoptive cell transfer (ACT) experiments

*In vivo* experiments were performed using antigen specific melanoma cell line B16-OVA (Bellone reference) that was maintained in culture in RPMI, 10%FBS, 1%PenStrep, 0,4mg G418 up to 5 passages prior to injection. C57B6/J mice were subcutaneously injected with 2x10<sup>5</sup> cells and tumor growth was monitored daily. 10 days post-injections, and once tumors had reached a measurable size, ACT was performed intravenously using 5x10<sup>6</sup> OT1 cells previously activated in the presence or absence of LA as previously described. Tumors were inspected and measured daily to construct a growth curve using the formula: Tumor volume= length x width<sup>2</sup>/2, where length represents the largest tumor diameter and width represents the perpendicular tumor diameter. On the day of analysis spleen, draining and non-draining lymph nodes and tumor were collected from each mouse, disaggregated to single cell suspension and used for flow cytometry analysis.

### Isolation and culture of primary human T lymphocytes

Peripheral blood mononuclear cells (PBMCs) were isolated from samples obtained from healthy donors or anonymous buffy coats (purchased as discarded material from the blood bank) of healthy donors using Ficoll density separation. CD8<sup>+</sup> T cells were obtained from PBMCs by negative magnetic selection. T lymphocytes were activated with immobilized Anti-human CD3 (2 µg/ml.) and anti-CD28 (2 µg/ml) antibodies and then expanded in complete RPMI 1640 medium (10% FBS, 1% NaPy, 1% Glutamine, 1% Pen/Strep) supplemented with 100 U/mL IL2. Cells were cultured for 48 hours in the presence or absence of LA. Resting cells were kept as control with no further activation stimulus provided.

### CAR-T cell engineering and GMP protocols

#### Cell lines

Neuroblastoma (NB)-derived cell line SHSY5Y, Burkitt's lymphoma cell line Raji and the immortalized human embryonic kidney 293T were obtained from DSMZ. The non-Hodgkin's Lymphoma (NHL)-derived cell line Karpas 299 was instead purchased from ECACC (Salisbury, United Kingdom). SHSY5Y and the 293T cell lines were maintained in culture with DMEM medium; the Karpas 299 and Raji cell lines were cultured with RPMI 1640 medium. All the cell lines were supplemented with 10% foetal bovine serum (FBS) and 2 mM glutamine. Cells were maintained in a humidified atmosphere containing 5% CO<sub>2</sub> at 37°C. All cell lines were routinely tested for mycoplasma and for surface expression of target antigens as well as authenticated by STR analysis (Eurofins Genomics, Ebersberg – Germany).

#### Isolation, generation and transduction of CAR T cells

Peripheral blood mononuclear cells (PBMC) were isolated from buffy coats obtained from healthy donors (University Hospital Würzburg, Würzburg, Germany) who signed a written informed consent, in accordance with rules set by the Institutional Review Board (Approval number 250/20-am), using Lymphocyte separation medium Ficoll. T lymphocytes were activated with immobilized OKT3 (1 mg/ml) and anti-CD28 (1 mg/ml) monoclonal antibody (mAb) in complete medium consisting of CTS OpTmizer T Cell Expansion medium supplemented with 2.5% human AB serum, 2 mM glutamine and with or without 100 µM/ml of LA, in a humidified atmosphere containing 5% CO<sub>2</sub> at 37°C. The day after activation, T cells were fed with recombinant human interleukin-7 (IL7, 500 U/ml) and -15 (IL15, 50 U/ml). Activated T cells were transduced on day 3 in 24-well plates pre-coated with recombinant human RetroNectin using a specific retroviral supernatant and the above-described cytokines. On day 5 after transduction, T cells were removed from RetroNectin and expanded in complete media.

#### Retroviral constructs

Three CAR constructs have been used in this study: a third generation CD30.CAR and GD2.CAR encoding for CD28.4-1bb.zeta-chain (ζ) and a second generation CD19.CAR encoding for 4-1bb.ζ. An additional retroviral vector encoding eGFP-Firefly-Luciferase (eGFP-FFLuc) was used in selected experiments to label tumor cells for *in vitro* co-culture and *in vivo* studies as previously described.

#### Co-culture assay

For co-culture experiments, NT, CD30.CAR, GD2.CAR or CAR.CD19 T lymphocytes cultured in presence or absence of LA were plated in 24-well plates at the indicated E:T ratios with GFP modified tumor cell lines (Karpas 299, CD30<sup>+</sup> tumor cell line; SHSY5Y, GD2<sup>+</sup> tumor cell line; Raji, CD19<sup>+</sup> tumor cell line). Following 5 days of incubation at 37°C, co-cultures were collected and analysed by FACS to detect residual tumor cells (GFP+) and T cells based on CD3 expression.

#### Live cell imaging staining

NT and CAR-T cells were collected and washed twice with phosphate buffered saline (PBS) supplemented with 1% of bovine serum albumin (BSA). T cells were then staining with CD45 BV421. CAR-T cell population was visualized by staining with 1A7 anti-idiotype CAR mAb (1 mg/ml), followed by APC-conjugated goat anti-mouse secondary antibody (1:500 in 1% BSA/PBS). In specific setting GFP modified tumors were used to redirect CAR T cells.

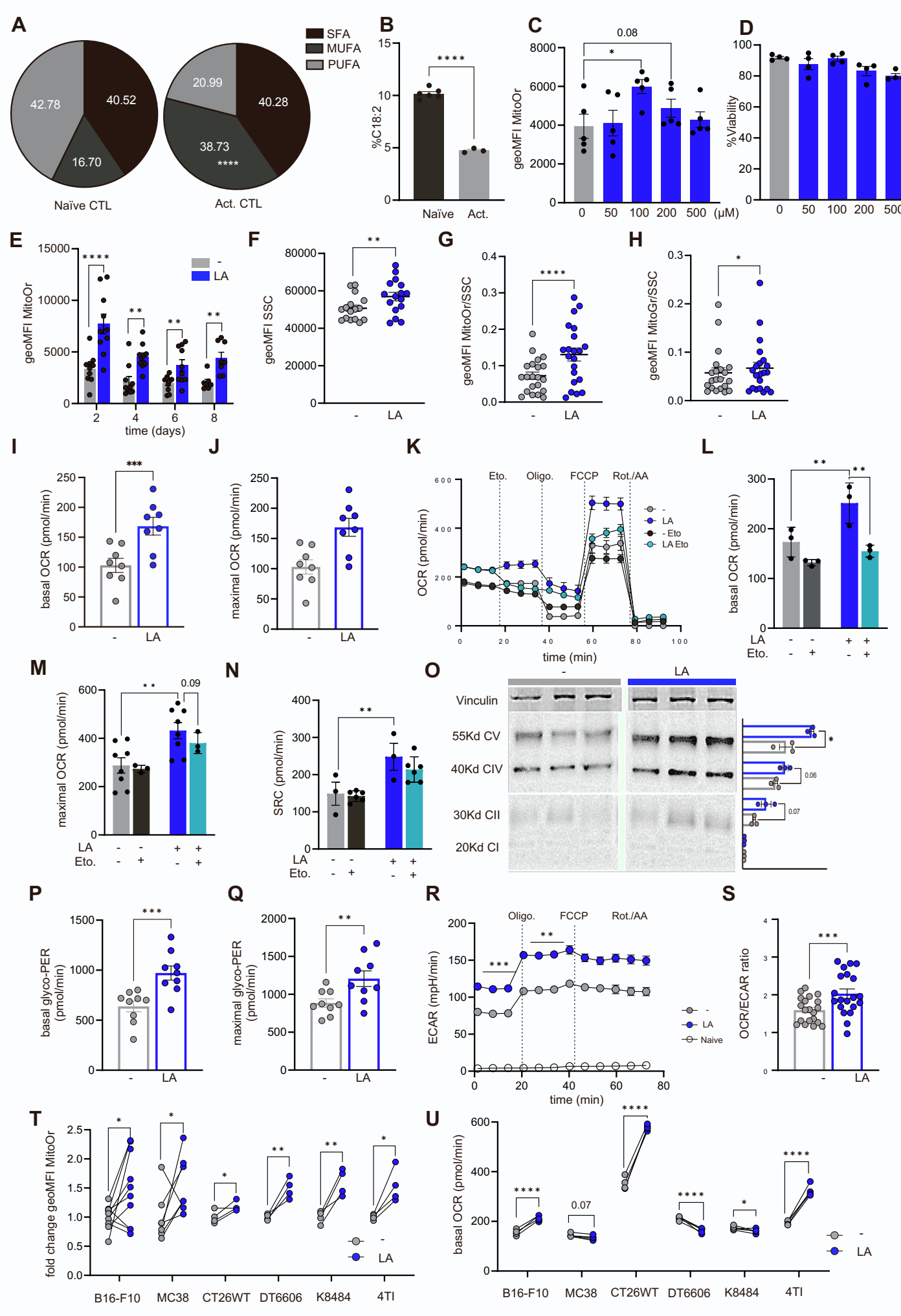
### QUANTIFICATION AND STATISTICAL ANALYSIS

Flow cytometry data was analysed using FlowJo v10.2. Western blots were quantified with ImageJ software. Statistical Analysis was performed using GraphPad Prism. Results are represented as mean ± standard error (SEM). Unless otherwise specified, paired t-Student test was used to compare LA-CTL and CTRLs. Normal distribution was evaluated using the Shapiro-Wilk test. Metabolomics data were normalized to cell count and/or protein content. Comparisons of more than two groups were calculated using one-way ANOVA with Tukey multiple comparison correction. All graphs show mean ± SEM were \*\*\*\* p-value < 0.0001, \*\*\* p-value < 0.001; \*\* p-value < 0.01, \* p-value < 0.05.

**Supplemental information**

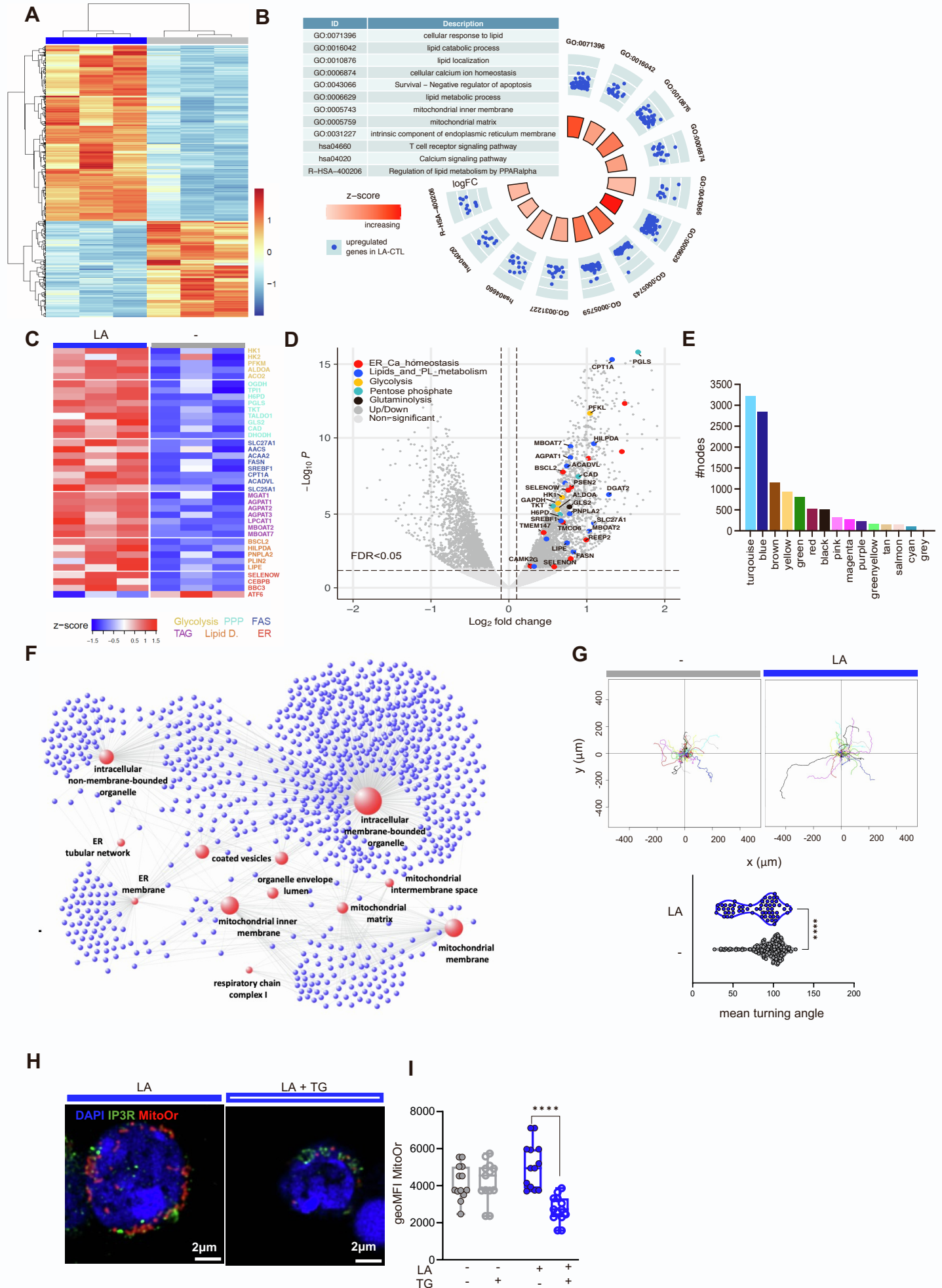
**Linoleic acid potentiates CD8<sup>+</sup> T cell  
metabolic fitness and antitumor immunity**

**Carina B. Nava Lauson, Silvia Tiberti, Paola A. Corsetto, Federica Conte, Punit Tyagi, Markus Machwirth, Stefan Ebert, Alessia Loffreda, Lukas Scheller, Dalia Sheta, Zeinab Mokhtari, Timo Peters, Ayush T. Raman, Francesco Greco, Angela M. Rizzo, Andreas Beilhack, Giovanni Signore, Nicola Tumino, Paola Vacca, Liam A. McDonnell, Andrea Raimondi, Philip D. Greenberg, Johannes B. Huppa, Simone Cardaci, Ignazio Caruana, Simona Rodighiero, Luigi Nezi, and Teresa Manzo**



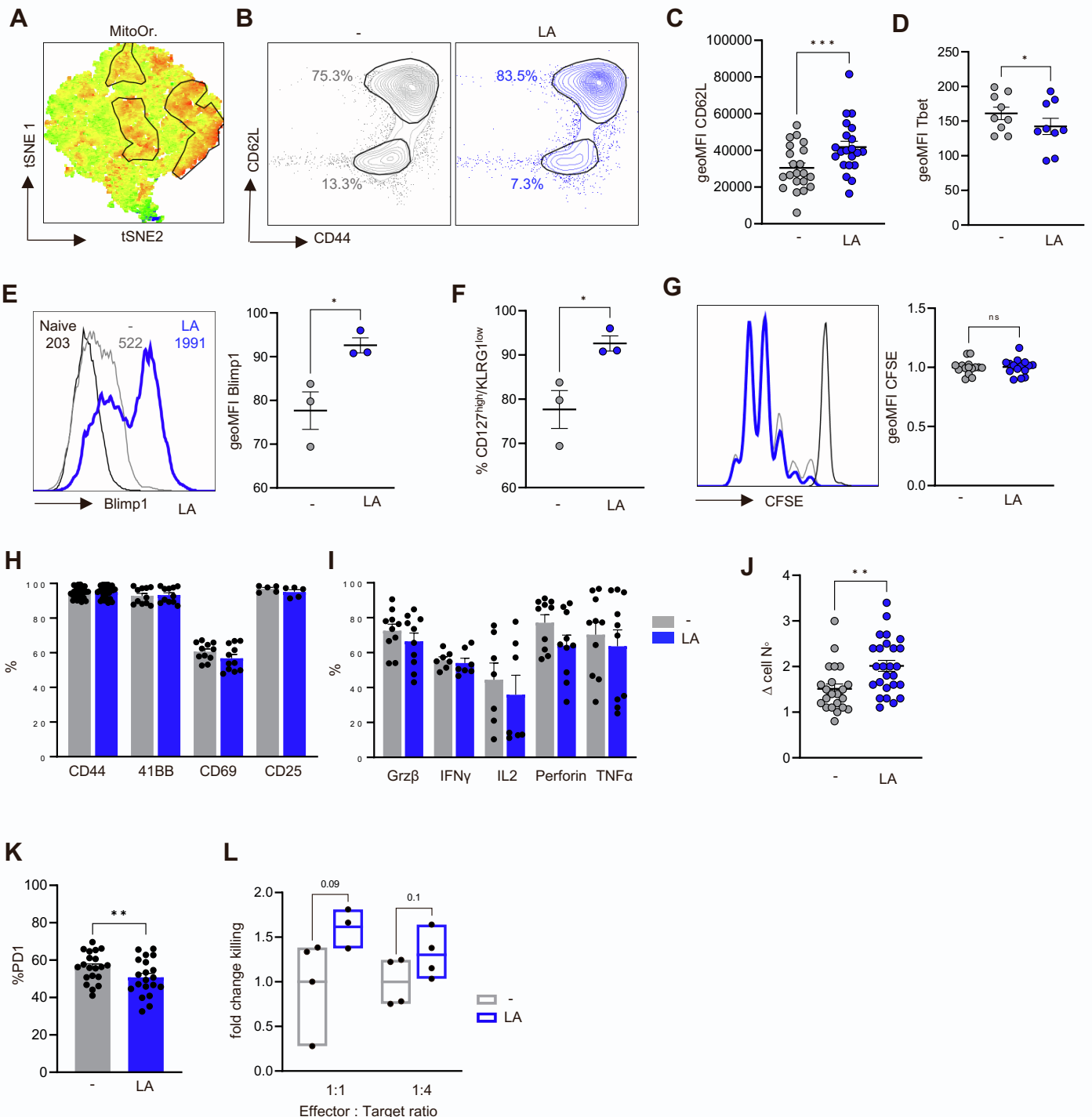
## **Supplementary figure 1. LA promotes mitochondrial rewiring in CTL. Related to Figure 1.**

(A-B) LS-MS quantification of SFA, MUFA and PUFA (A) and C18:2 (B) in naïve (n=5) and activated (n=3) CTL. MitoOr. staining (C) and viability percentage (D) upon LA titration (n=4).  
(E) MitoOr. staining in long term culture (n=6/10; 3 independent experiments).  
SSC values (F) were used to normalize MitoOr (G) and MitoGr (H) (n=16/20; 5 independent experiments).  
(I-J) CTL metabolic profile: basal (I) and maximal (J) OCR (n=8/12; 3 independent experiments).  
(K-N) FAO dependency test: OCR (K-M) and SRC (N). n=4.  
(O) OXPHOS representative western blot (n=3; 2 independent experiments).  
(P-R) Glycolytic activity: basal (P) and maximal (Q) PER (n=9; 3 independent experiments), as well as ECAR (R, n=4, representative of 5 independent experiments).  
(S) OCR/ECAR ratio (n=20; 5 independent experiments).  
(T-U) LA effect on tumor cell lines. MitoOr. (T) staining and basal OCR (U).  
Data are represented as mean  $\pm$  SEM. Paired, two-tailed Student's t test \*p < 0.05, \*\*p < 0.01, \*\*\*p < 0.001, \*\*\*\*p < 0.0001.



## **Supplementary figure 2. LA favors ER-Mitochondria network in CTL. Related to Figure 2.**

- (A) Topmost variable genes scoring from unsupervised clustering analysis (n= 3).  
(B) Top biological processes upregulated within total DEGs.  
(C) Heatmaps representing genes related to glycolysis, PPP, FAS, TAG, lipid droplets and ER.  
(D) Volcano plot highlighting most representative genes for ER-Ca<sup>2+</sup> homeostasis, lipids and PL metabolism, glycolysis, PPP and glutaminolysis pathways.  
(E) Modules identified from WGCNA and respective DEG number.  
(F) GO cellular components network from blue module.  
(G) Rose plots and mean turning angle based on live cell tracking assays.  
(H-I) Effect of TG on MitoOr measured by confocal microscopy (H) and flow cytometry (I).  
Data are represented as mean ± SEM. Paired (H) or unpaired (F), two-tailed Student's t test \*\*\*p < 0.0001.



**Supplementary figure 3. LA pushes memory differentiation in CTL. Related to Figure 2 and 4.**

(A) tSNE representation showing MitoOr. MFI (n=5).

(B-F) CTL memory phenotype assessed as: representative FACS plot showing CD44<sup>high</sup>/CD62L<sup>high</sup> (B) and CD62L (C, n=21, 5 independent experiments), Tbet (D, n=9; 3 independent experiments), Blimp1 (E, n=14; 4 independent experiments) and CD127<sup>high</sup>/KLRG1<sup>low</sup> (F) expression assessed by flow cytometry.

(G) CFSE profile (n=14; 4 independent experiments).

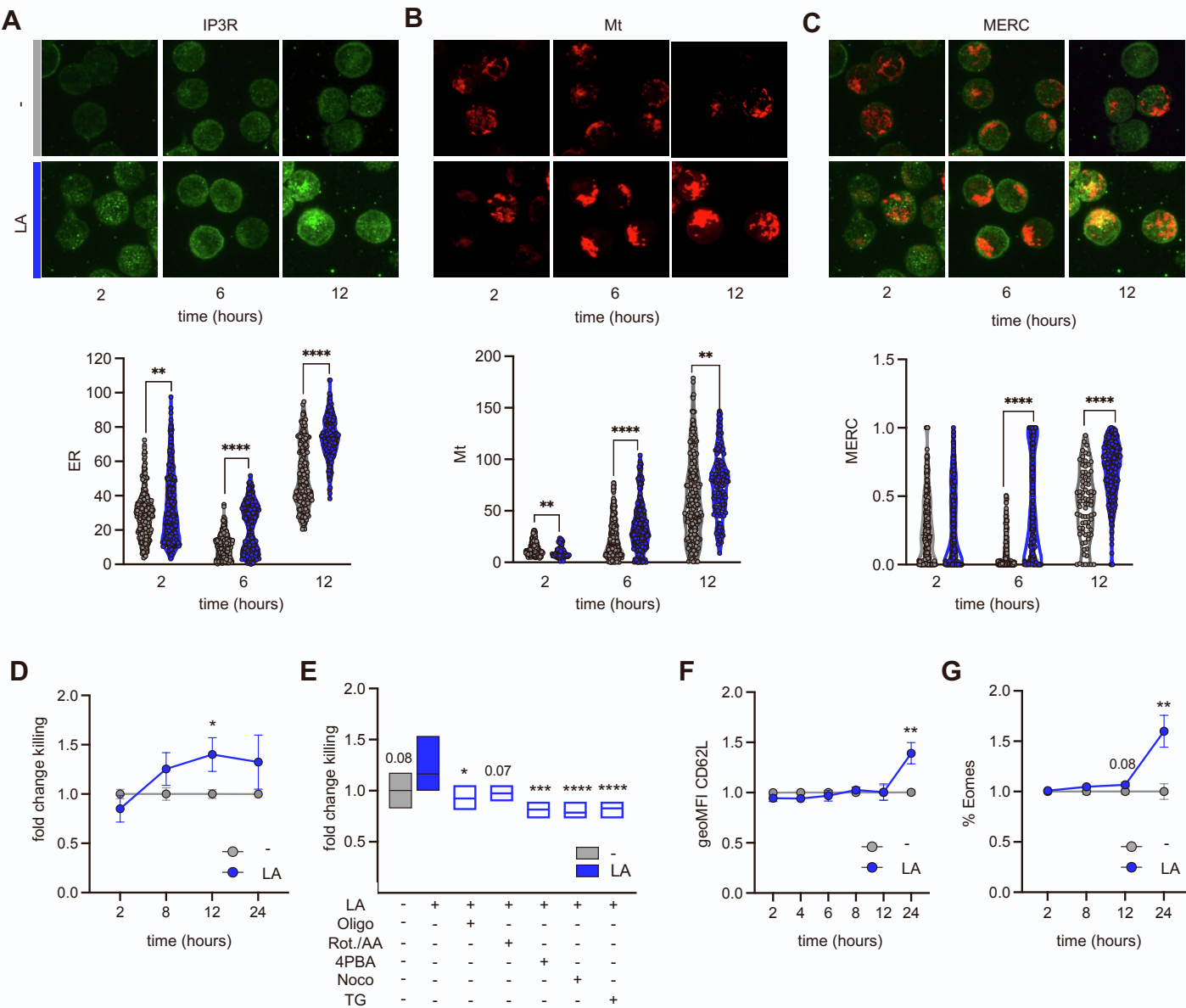
(H-I) Activation status measures as: canonic activation markers (H) and effector cytokines (I).

(J) Fold change in cell numbers after 48 hours of activation (n=26; 5 independent experiments).

(K) Percentage of PD1 positive cells (n=20; 5 independent experiments).

(L) Effector function assessed as killing assays 48 hours post-activation (n=4).

Data are represented as mean ± SEM. Paired, two-tailed Student's t test \*p < 0.05, \*\*p < 0.01, \*\*\*p < 0.001, \*\*\*\*p < 0.0001.



**Supplementary figure 4. Dynamic and fate of LA-redirected CTL. Related to Figure 4.**

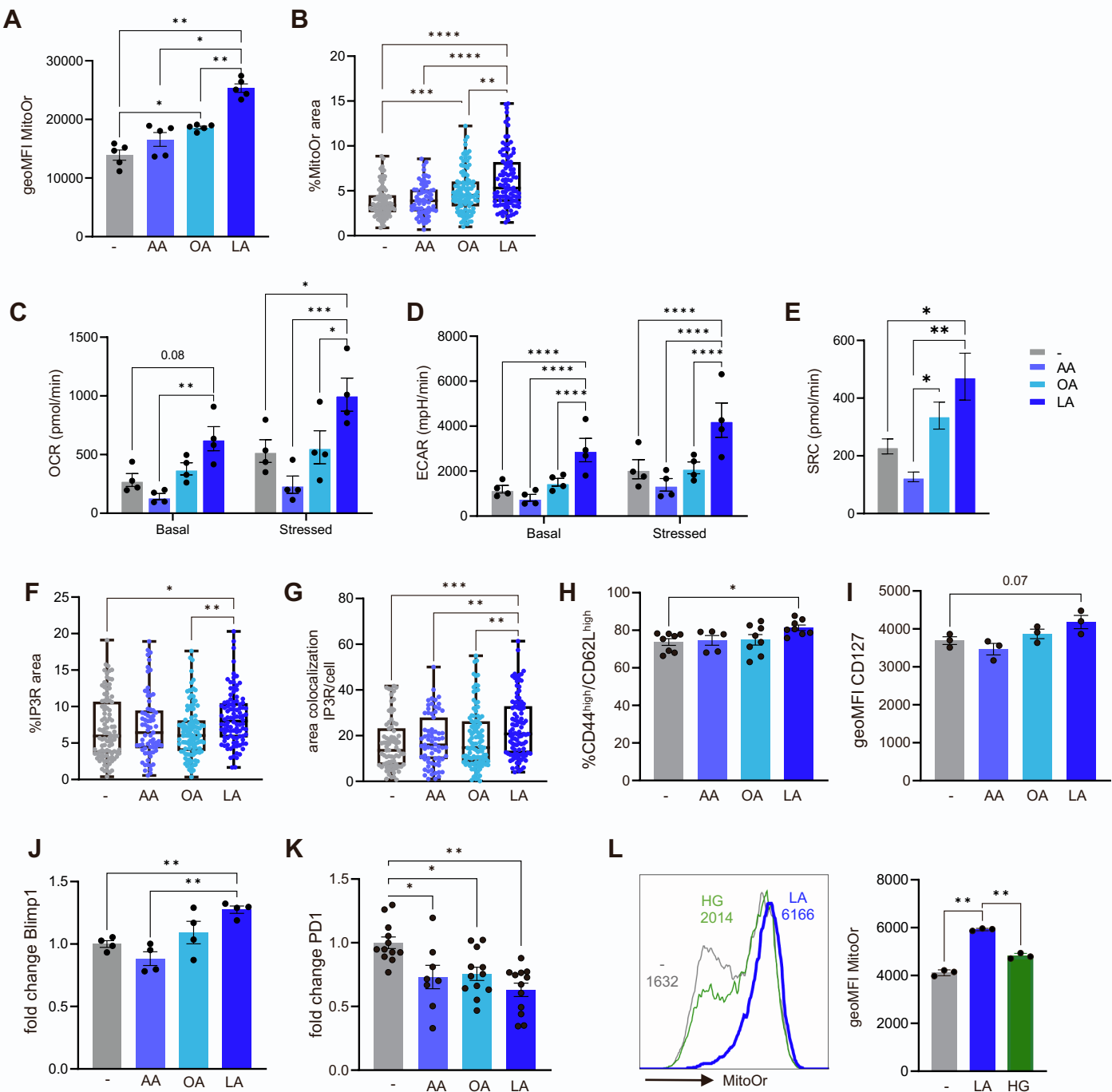
(A-C) Representative confocal images (top panels) and respective quantification (bottom graphs) of kinetics experiments for IP3R (A), MitoOr (B) and MAM formation (C).

(D) Effector functions assessed by killing assay (n=7).

(E) Effect of mitochondrial activity blockage (Oligo and Rot./AA) and MAM disruption (4PBA, Noco and TG) on CTL effector function (n=3/5).

(F-G) Kinetics on memory phenotype assessed by CD62L (F) and Eomes (G) expression.

Data are represented as mean  $\pm$  SEM. Paired, two-tailed Student's t test (A,B,C and D) or one-way ANOVA using LA as control group (E) \*p < 0.05, \*\*p < 0.01, \*\*\*p < 0.001



**Supplementary figure 5. LA has a unique role in regulating CTL responses. Related to Figure 1 and 2.**

(A-B) MitoOr. staining MFI -calculated by FACS - (A, n=5) and area -calculated by confocal microscopy (B, n=5).

(C-E) Metabolic profile assessed as: OCR (C), ECAR (D) and SRC (E). n= 4.

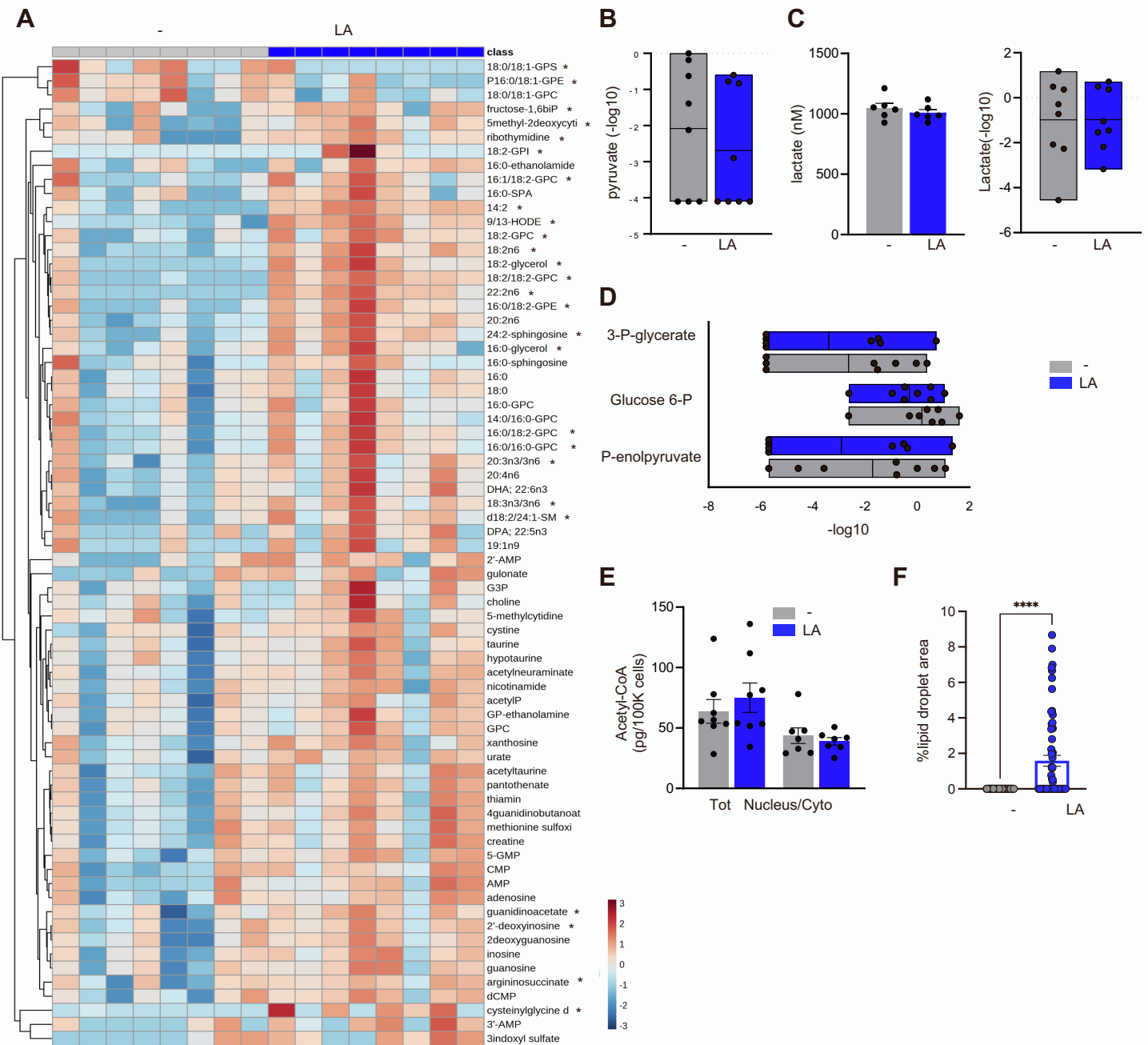
(F-G) IP3R area (F) and MAM quantification (G) by confocal microscopy (n=5; 2 independent experiments).

(H-K) Memory phenotype assessed as CD44<sup>high</sup>/CD62L<sup>high</sup> (H), CD127 (I) and Blimp1 (J),

(K) PD1 expression on different LC-FAs.

(L) MitoOr. staining on cells cultured in high-glucose conditions.

Data are represented as mean  $\pm$  SEM. Paired, two-tailed Student's t test \*p < 0.05, \*\*p < 0.01, \*\*\*p < 0.001, \*\*\*\*p < 0.0001.

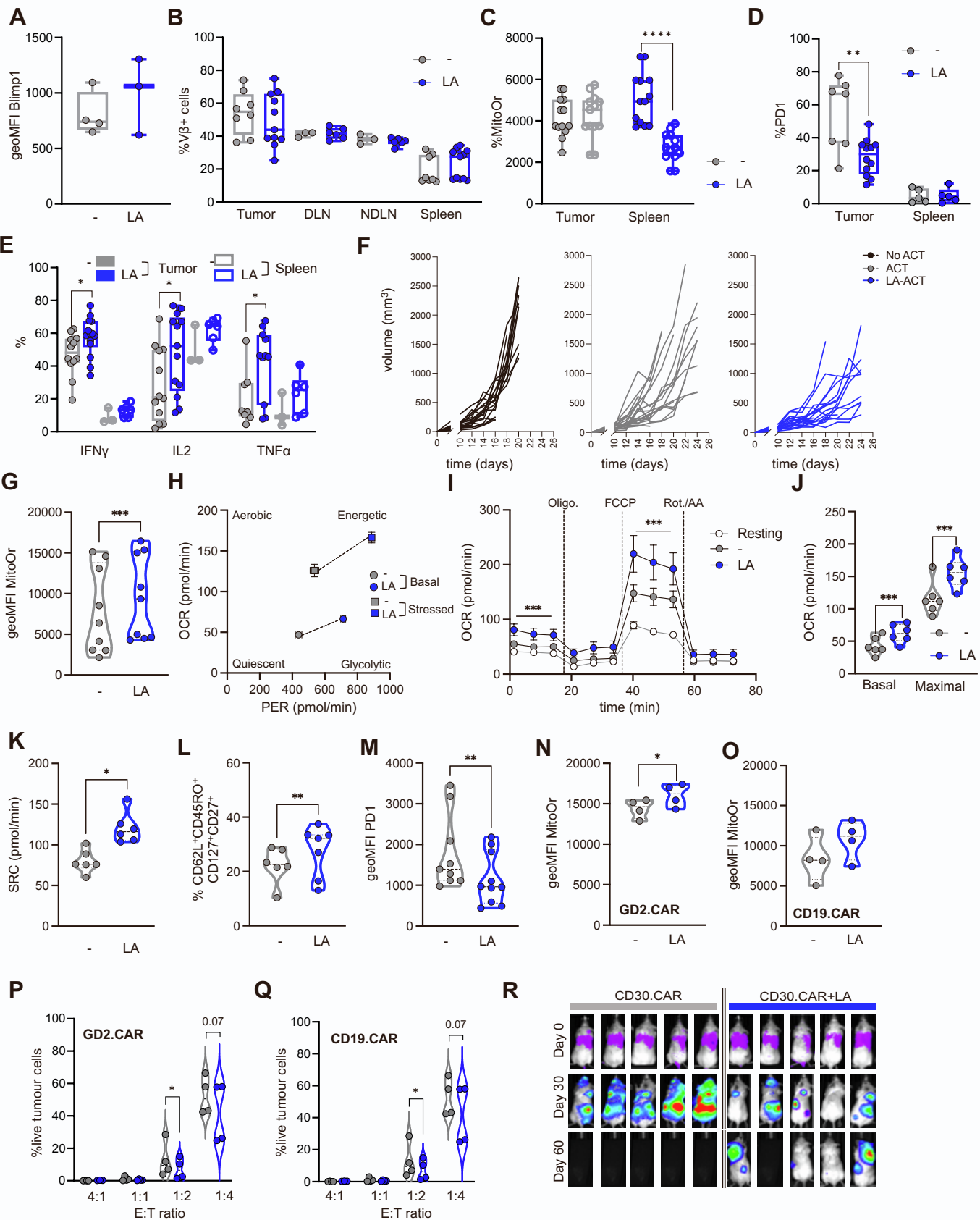


**Supplementary figure 6. Metabolomic profile of CTL upon LA treatment. Related to Figure 5.**

(A) Metabolomics heatmap showing top 80 metabolites (n=8).

(B-E) Quantification of metabolites and metabolic intermediates: pyruvate (B), lactate (C), PPP (D) and acetyl-CoA (E).

(F) Lipid droplet quantification by TEM (n=3).



## **Supplementary figure 7. LA-CTL improves ACT efficacy. Related to Figure 6 and 7.**

- (A) Blimp1 expression.
  - (B) Percentage of adoptively transferred CTL.
  - (C-E) Phenotypic characterization: MitoOr. (C), PD1 (D) and effector cytokines (E).
  - (F) Spider plots representing tumor growth curves.
  - (G-K) Metabolic characterization of human CD8 T cells (n=6/10; 3 independent experiments): MitoOr. (G), energetic map (H), OCR (I-J) and SRC (K).
  - (L-M) Phenotypic characterization of human CD8 T cells: percentage of TCM (L), expression levels of PD1(M).
  - (N-O) MitoOr of CAR-T cells: GD2 (N) and CD19 (O).
  - (P-Q) Long term killing assays in GD2 (P) and CD19 (Q) CAR T cells.
  - (R) Bioluminescence images assessing tumor burden.
- Data are represented as mean  $\pm$  SEM. B, C and D show percentages within adoptively transferred CTL 14 days post-ACT. Statistics are based on paired (g-) or unpaired (A-F and R), two-tailed Student's t test \*p < 0.05, \*\*p < 0.01, \*\*\*p < 0.001, \*\*\*\*p < 0.0001.